

PROBABILISTIC MATERIAL MODELING OF SELECTIVE LASER MELTED
A357 ALUMINUM ALLOY SUBJECTED TO LASER SHOCK PEENING

by

Jagannathan Shankar Mahadevan

APPROVED BY SUPERVISORY COMMITTEE:

Arif S. Malik, Chair

Dong Qian

Ill Ryu

Copyright © 2017

Jagannathan Shankar Mahadevan

All rights reserved

To my family: Mom, Dad, Madhumitha and Satish

PROBABILISTIC MATERIAL MODELING OF SELECTIVE LASER MELTED
A357 ALUMINUM ALLOY SUBJECTED TO LASER SHOCK PEENING

by

JAGANNATHAN SHANKAR MAHADEVAN, BE

THESIS

Presented to the Faculty of
The University of Texas at Dallas
in Partial Fulfillment
of the Requirements
for the Degree of

MASTER OF SCIENCE IN
MECHANICAL ENGINEERING

THE UNIVERSITY OF TEXAS AT DALLAS

August 2017

ProQuest Number:10675272

All rights reserved

INFORMATION TO ALL USERS

The quality of this reproduction is dependent upon the quality of the copy submitted.

In the unlikely event that the author did not send a complete manuscript and there are missing pages, these will be noted. Also, if material had to be removed, a note will indicate the deletion.



ProQuest 10675272

Published by ProQuest LLC (2017). Copyright of the Dissertation is held by the Author.

All rights reserved.

This work is protected against unauthorized copying under Title 17, United States Code Microform Edition © ProQuest LLC.

ProQuest LLC.
789 East Eisenhower Parkway
P.O. Box 1346
Ann Arbor, MI 48106 – 1346

ACKNOWLEDGMENTS

I would like to express my sincere appreciation to my advisor, Dr. Arif S. Malik, for motivating me to participate in academic research and for his immense knowledge and guidance in my area of concentration. I humbly extend my thanks to my committee members Dr. Dong Qian and Dr. Ill Ryu for all their valuable suggestions in this research. Without the support of Coventry University, this work would not have been possible to complete on time. Special thanks to Dr. Pratik Shukla and Dr. Suraiya Zabeen for the same. I would also like to acknowledge and extend my heartfelt gratitude to the faculties and staffs of the mechanical engineering department, UTD for offering me a full tuition waiver along with a teaching assistantship position and allowing me to do research. Special thanks to Dr. Dani Fadda who ensured I was financially stable throughout the Summer of 2017 and allotted flexible work hours for me to complete my thesis on time. I also have a deep sense of gratitude to my fellow colleague, Mohammad I. Hatamleh, for not only being a helpful senior in research but also a very good friend. I am thankful to my room mates for making me feel at home, far away from home. The last few games in fifa has been very challenging indeed. Finally, I am extremely thankful to my family who have always believed and seen a future in me. If not for my family, I would not have achieved this.

July 2017

PROBABILISTIC MATERIAL MODELING OF SELECTIVE LASER MELTED
A357 ALUMINUM ALLOY SUBJECTED TO LASER SHOCK PEENING

Jagannathan Shankar Mahadevan, MS
The University of Texas at Dallas, 2017

Supervising Professor: Arif S. Malik, Chair

Various processing parameters in Selective Laser Melting (SLM) such as scan speed, hatch distance, substrate temperature, *etc.*, have significant impact on the residual stresses present in the print. Compressive residual stresses induced by Laser Shock Peening (LSP) enhances the fatigue life of various metallic components and their alloys. Considering the presence of tensile residual stresses on A357 Aluminum SLM specimens due to the dispersion of eutectic silicon particles, LSP is applied to induce compressive residual stresses. Efficient numerical simulation of LSP is achieved using the Single Explicit Analysis using Time-dependent Damping (SEATD) technique. Conventionally, the material model used in LSP simulation employs deterministic parameters for residual stress prediction. The residual stress distribution predicted by these deterministic parameters are prone to be inaccurate even for similar LSP configurations due to the intrinsic uncertainties associated with the material itself. Hence, a joint random field for the material model parameters for the high strain rate LSP process is developed based on a probabilistic approach known as Bayesian Inference. The working technique of Bayesian Inference process for material model calibration is demonstrated using a set of assumed residual stress data. The calibrated material model parameters are then used in simulating a “candy-bar” coupon subjected to different LSP patterns. Conventionally casted A357 specimens are processed with a similar technique with

an aim of quantifying the difference in residual stress distribution as a result of varying manufacturing methodology. The results reveal that the finely calibrated material model parameters using Bayesian Inference predicts the assumed experimental residual stress field with a reasonable accuracy.

TABLE OF CONTENTS

| | |
|---|-----|
| ACKNOWLEDGMENTS | v |
| ABSTRACT | vi |
| LIST OF FIGURES | x |
| LIST OF TABLES | xii |
| CHAPTER 1 INTRODUCTION | 1 |
| 1.1 Additive Manufacturing | 1 |
| 1.2 Laser Shock Peening | 2 |
| 1.3 Laser Shock Peening on Selective Laser Melted Specimens | 4 |
| 1.4 Research need | 6 |
| CHAPTER 2 LASER SHOCK PEENING - EXPERIMENTAL SETUP | 9 |
| 2.1 Sample preparation | 9 |
| 2.2 Laser peening configuration | 12 |
| CHAPTER 3 LASER SHOCK PEENING MODEL FOR FINITE ELEMENT SIMULATION | 19 |
| 3.1 The Single Explicit Analysis using Time Dependent Damping Method | 19 |
| 3.1.1 Plasma Pressure Model | 21 |
| 3.1.2 Material model | 24 |
| CHAPTER 4 UNCERTAINTY QUANTIFICATION OF MATERIAL MODEL USING BAYESIAN INFERENCE | 27 |
| 4.1 Introduction | 27 |
| 4.2 Probabilistic Distribution of Johnson-Cook parameters | 28 |
| 4.2.1 Surrogate Modeling | 29 |
| 4.2.2 Likelihood function | 31 |
| 4.2.3 Posterior Probability | 32 |
| 4.3 Extending Bayesian Inference across Multiple Experimental Dimensions | 32 |
| 4.4 Material Model Calibration of Casted and SLM A357 | 33 |
| 4.4.1 Multidimensional Extension | 38 |

| | | |
|---------------------|---|----|
| CHAPTER 5 | RESIDUAL STRESS DISTRIBUTION FOR MULTIPLE LSP SHOTS | 43 |
| CHAPTER 6 | CONCLUSION | 49 |
| APPENDIX | EXPERIMENTAL APPARATUS | 50 |
| A.1 | Beam Path | 50 |
| A.2 | Beam Splitter and Beam Tap | 51 |
| A.3 | Fast Photodetector and Laser Energy Meter | 52 |
| REFERENCES | | 55 |
| BIOGRAPHICAL SKETCH | | 61 |
| CURRICULUM VITAE | | |

LIST OF FIGURES

| | | |
|-----|---|----|
| 1.1 | Laser Shock Peening (LSP) - Schematic | 3 |
| 1.2 | In-depth Residual Stress Distribution for SLM-LSP Specimens (Kalentics et al., 2017) ©2017 Reprinted with permission from <i>Elsevier</i> | 5 |
| 2.1 | Three Point Bend Candy-bar Coupon with Cross Section (All dimensions are in <i>mm</i>) | 10 |
| 2.2 | Polished SLM and Casted A357 Candy-bar Coupons | 11 |
| 2.3 | Experimental Setup - Schematic | 12 |
| 2.4 | Experimental Setup - Laser lab | 13 |
| 2.5 | 2-D Laser Spatial Distribution | 14 |
| 2.6 | 3-D Laser Beam | 14 |
| 2.7 | Laser Temporal Distribution | 15 |
| 2.8 | LSP Configuration for Material Model Calibration (all dimensions are in <i>mm</i>) | 17 |
| 2.9 | Sliced Candy-bar Specimen with LSP Affected Zone | 17 |
| 3.1 | Inputs for the SEATD Technique | 20 |
| 3.2 | Plasma Thickness | 23 |
| 3.3 | Plasma Pressure | 24 |
| 4.1 | Bayesian Inference of JC parameters | 30 |
| 4.2 | Residual Stress - Prior PMF | 35 |
| 4.3 | SLM Residual Stress (<i>RS-0</i>) - Iteration 1 | 36 |
| 4.4 | SLM Residual Stress (<i>RS-0</i>) - Iteration 3 | 37 |
| 4.5 | Longitudinal Stress - Radial Distribution for SLM Specimens | 39 |
| 4.6 | Longitudinal Stress - Radial Distribution for Casted Specimens | 40 |
| 4.7 | Longitudinal Stress for SLM Specimens with Spatially Calibrated JC Parameters | 41 |
| 4.8 | Longitudinal Stress for Casted Specimens with Spatially Calibrated JC Parameters | 42 |
| 5.1 | Pattern - 1 with circular LSP shots (100% coverage of laser peen area) (all dimensions are in <i>mm</i>) | 43 |
| 5.2 | Pattern - 2 with circular LSP shots (Consecutive shots) (all dimensions are in <i>mm</i>) | 44 |
| 5.3 | Laser Shock Peened Candybar Coupons | 45 |
| 5.4 | Candybar - FEM Simplification | 45 |

| | | |
|-----|--|----|
| 5.5 | Compressive Stress Field due to Pattern-1 | 46 |
| 5.6 | Residual Stress Distribution through the Path shown in Fig. 5.5 | 47 |
| 5.7 | Compressive Stress Field due to Pattern-2 | 48 |
| 5.8 | Residual Stress Distribution through the Path shown in Fig. 5.7 | 48 |
| A.1 | Laser Spatial Distribution - Apparatus | 51 |
| A.2 | Quanta-Ray Laser Beam Spatial Distribution using <i>BeamGage</i> | 52 |
| A.3 | Laser Temporal Distribution | 53 |
| A.4 | Laser Energy | 54 |

LIST OF TABLES

| | | |
|-----|---|----|
| 2.1 | Chemical Composition of Casted A357 | 9 |
| 2.2 | Properties of A357 Aluminum Alloy | 10 |
| 2.3 | LSP Process Parameters | 16 |
| 2.4 | Recorded LSP Parameters for Material Modeling | 18 |
| 3.1 | Parametric Constants for Plasma Pressure Modeling | 23 |
| 3.2 | Johnson-Cook Parameters for A357 Alloy adapted from (Gupta et al., 2014) | 26 |
| 4.1 | Assumed Test Data for Experimental Residual Stress (for BI Demonstration) | 34 |
| 4.2 | LHS Domain | 35 |
| 4.3 | Calibrated Johnson-Cook Parameters for $RS-0$ | 38 |
| 4.4 | Bayesian Inference Output for $RS-0.5$, $RS-1$ and $RS-1.5$ | 39 |
| 4.5 | Calibrated Johnson-Cook Parameters for the Residual Stress Field | 41 |
| 5.1 | Laser Shock Peening - Pattern | 44 |

CHAPTER 1

INTRODUCTION

This chapter gives a detailed introduction to two different yet pivotal topics involved in this research, *i.e.*, Additive Manufacturing (AM) and Laser Shock Peening (LSP). A brief history of both the processes followed by the prevalent state of the art technology is explained in Section 1.1 and 1.2. A concise literature review on the integrated laser shock peening - selective laser melting process is explained in Section 1.3. A detailed rationale for laser shock peening on selective laser melted specimens and the need for current research with thesis organization is explained in Section 1.4.

1.1 Additive Manufacturing

Per the American Society for Testing and Materials, Additive Manufacturing (AM) is defined as a process of joining materials to make objects from 3D model data, usually layer upon layer, as opposed to subtractive manufacturing methodologies. Synonyms: additive fabrication, additive processes, additive techniques, additive layer manufacturing, layer manufacturing, and freeform fabrication (ASTM-F2792, 2012). Additive manufacturing is capable in revolutionizing current manufacturing logistics by enhancing parts on demand production with significant cutback in production cost, fabrication time and carbon footprint (Frazier, 2010, 2014; Baumers et al., 2010). Remote manufacturing of functional parts and better output due to reduced geometrical constraints has drawn the attention of automotive and aerospace industries towards additive manufacturing (Frazier, 2014). Surgical instruments used in bio-medical industries can be fabricated rather quickly at low cost thereby reducing patient wait time during emergencies (Emelogu et al., 2016; Murr et al., 2010). Additive manufacturing is briefly classified into powder bed systems, powder feed systems and wire feed systems (Frazier, 2014). Selective Laser Melting (SLM) (Bremen et al., 2012; Rombouts

et al., 2006; Agapovichev et al., 2016; Rao et al., 2016; Aversa et al., 2017) is a powder bed system - additive manufacturing process which builds each layer by irradiating the metal powder with a laser beam. Various metallic elements and their alloys such as titanium, aluminum, steel, *etc.*, are used in selective laser melting (Rombouts et al., 2006; Agapovichev et al., 2016).

Although additive manufacturing provides several benefits compared to traditional manufacturing methodologies, its true potential is yet to be realized. Uncertainty exists between various structural parts produced by additive manufacturing due to differing surface morphology and machine to machine variability (Selcuk, 2011). Various process parameters such as build procedure, scan speed, laser power, layer thickness and substrate temperature adds to the structure uncertainty. Also, high heating and cooling rates during the process induces thermal fluctuations resulting in tensile residual stresses (Frazier, 2014; Shamsaei et al., 2015).

Active research is currently underway to address the relationship between various processing parameters in selective laser melting and the resulting microstructure, porosity and mechanical properties (Rao et al., 2016; Trosch et al., 2016; Attar et al., 2014; Kempen et al., 2011; Aboulkhair et al., 2014). Efficient optimization of the additive manufacturing process might possibly yield fine structures with reduced porosity and improved material properties.

1.2 Laser Shock Peening

Laser shock peening (LSP) is a modern surface engineering treatment which is extensively used to impart beneficial compressive residual stresses on the target specimen. It is often compared with other surface enhancement techniques such as shot peening, waterjet peening, *etc.* While shot peening is widely utilized in most industries, the latter is currently under extensive research (Arola et al., 2006; Singh, 2009). Aviation and aerospace industries make

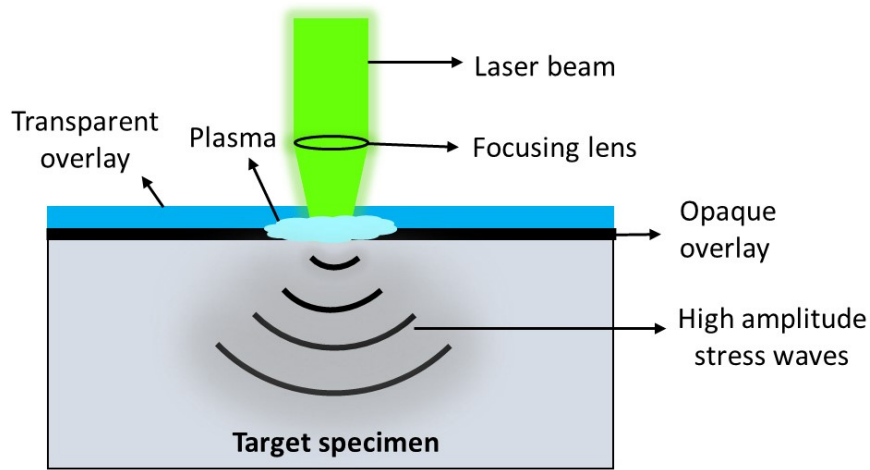


Figure 1.1. Laser Shock Peening (LSP) - Schematic

use of this process to extend the fatigue life of various metals and alloys (Fairand et al., 1972; Clauer et al., 1983).

During laser peening, the specimen is generally covered with an opaque overlay (black paint or aluminum tape) and a transparent medium (commonly water or quartz crystal) as shown in Fig. 1.1. The incident laser beam ($1-10 \text{ GW/cm}^2$) on the work piece, through the overlays, ablates the specimen to produce plasma as a result of reaching extremely high temperatures (10000°C) at low deposition times (order of ns). The plasma is restricted within the transparent overlay to produce high plasma pressure on the specimen surface. The induced plasma pressure is then transmitted through the specimen as shock waves to create a compressive residual stress field.

Numerous processing parameters involved in laser peening such as incident laser power density, laser spatial and temporal profiles, overlap percentage, *etc.*, along with the complexity of laser system and manual labor involved does not only make the process expensive but also retards its growth in the industry. To address this issue, researchers initially made use of computers to develop analytical techniques in predicting the residual stresses due to laser peening (Braisted and Brockman, 1999). Two-dimensional axisymmetric finite element

(FEM) model subjected to a uniform spatial and triangular ramped temporal pressure model was used for LSP simulation with dynamic explicit analysis for shock loading and static implicit analysis for static equilibrium. Various finite element techniques for laser peening are further being developed to address the issue of computation cost and time. The recently developed single explicit analysis using time-dependent damping (SEATD) uses dynamic explicit analyses for both shocking and variable damping rather than the conventionally used explicit-implicit approach in order to reduce computation time (Hasser et al., 2016).

Currently, with advancement in computational technology - different optimization techniques are quite often used to obtain the most beneficial residual stress field leading to favorable mechanical properties (Hasser et al., 2016; Spradlin, 2011; Bhamare et al., 2013). Continuous research is actively underway to also automate the process of laser peening. Thus, with the prediction of favorable process parameters obtained through multiple simulations, combined with experimental validation tests, laser peening has the potential to develop into an efficient, cheap and time-saving surface enhancement technique.

1.3 Laser Shock Peening on Selective Laser Melted Specimens

Whilst the treatment of selective laser melted specimens with laser shock peening is a relatively new process, some research with regards to this integration is recently documented. Published work by researchers involved the study of laser peening affected residual stress field on selective laser melted specimens (Kalentics et al., 2017). Two different grades of selective laser melted steels. *i.e.*, 15-5 martensitic precipitation hardenable PH1 steel and austenitic 316 L steel were laser peened and the corresponding residual stress distribution is compared with the as built unpeened specimens as shown in Fig. 1.2. Fig. 1.2 shows the in-depth residual stress distribution for the as-built (AB) and non-coated (NC) specimens with 40% and 80% overlap conditions for laser shots having 1 mm diameter (Kalentics et al.,

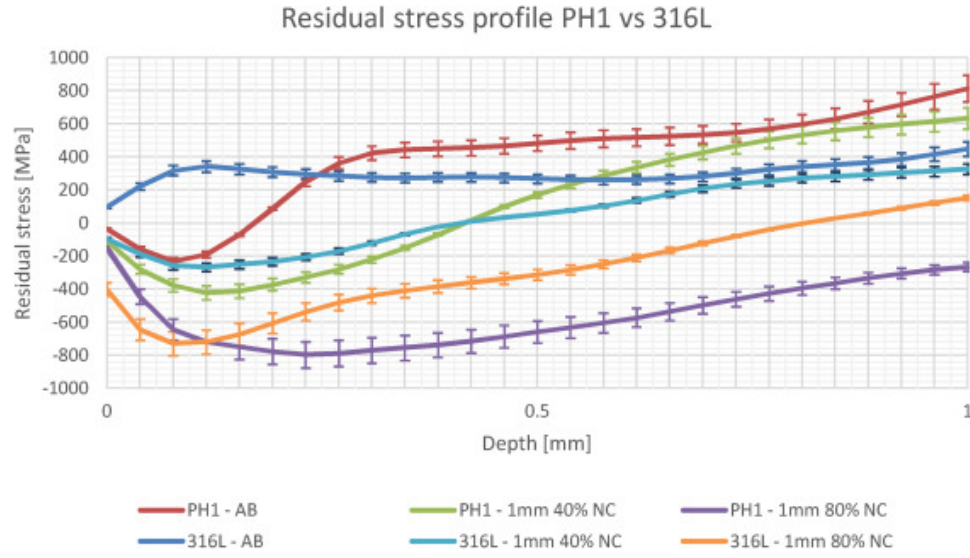


Figure 1.2. In-depth Residual Stress Distribution for SLM-LSP Specimens (Kalentics et al., 2017) ©2017 Reprinted with permission from *Elsevier*

2017). Also, the effect of various laser peening parameters such as spot overlap, spot diameter and the type of sacrificial coating used to achieve the goal of transforming the detrimental tensile residual stresses into beneficial compression on the selective laser melted specimens are studied.

A new process known as 3D-LSP in which the specimen is intermittently laser peened at the SLM build stage is introduced (Kalentics et al., 2017). Increased depth of compressive residual stress is noticed with a corresponding increase in the number of SLM layers between LSP. It is also observed that the 3-D LSP process increases both the magnitude and depth of compressive residual stresses. Comparison of 3D-LSP and conventional LSP process reveals that the former with a reduced spot diameter and pulse energy produces deeper compressive residual stresses than the latter with a larger spot and energy.

A coupled numerical tool for the finite element simulation of SLM-LSP process to obtain the eventual residual stress field on the 3-D printed specimen (hybrid AM formulation) is recently developed (Sealya et al., 2016). Thermal stresses induced on the specimen due to high temperature gradient experienced by the specimen through the build phase affects the

compressive residual stresses due to laser peening. The influence of SLM-layer thickness and LSP-peak pressure on the final residual stress distribution is studied. The numerical results reveal that the thermal loads resulting due to thicker layers are of no importance to the final residual stress whereas thinner layers necessitate a higher magnitude of laser peening pressure for deeper compression.

Through efficient optimization of the integrated laser shock peening - selective laser melting process conditions, it is therefore possible to tailor the final mechanical properties of additive manufactured elements as per need or application.

1.4 Research need

During the process of selective laser melting, each printed layer is subsequently allowed to cool in order to obtain a solid structure prior to printing the next layer. Previous studies show that in selective laser melting of metals, the molten layer contracts during the liquid-solid transformation phase while the solidified metal layer underneath the molten metal layer inhibits contraction (Kruth et al., 2012; Casavola et al., 2008). As a result, tensile residual stresses are developed through the depth and gets accumulated with each layer.

The effect of residual stress on the fatigue strength and fatigue crack growth rate (FCGR) is an interesting topic of research. The influence of residual stress on the fatigue strength for two different grades of high strength steel is extensively studied (Shiozaki et al., 2015). Multiple holes were punched on the specimen with varying punch conditions to induce residual stresses. The punched specimens were then subjected to plane-bending displacement controlled fatigue tests and the fatigue performance of the as-punched and heat-treated specimens with varying punch conditions are compared. The fatigue test results reported a higher fatigue strength for the specimens processed with punch conditions favoring minimum tensile stresses.

Recent studies involved the influence of processing parameters of selective laser melting such as scan speed and laser power on the microstructure and mechanical properties of A357 aluminum alloys (Rao et al., 2016). It was reported that the microstructure of A357 alloy and the dispersion of eutectic silicon particles in the A357 matrix significantly affects its tensile properties. During plastic deformation, multiple cracks due to surface tension are observed to initiate at regions comprising a higher concentration of silicon particles. Also, (Aversa et al., 2017) studied the significance of substrate temperature and post-processing heat treatment on selective laser melted A357 and observed strong anisotropy with notable changes in mechanical properties.

(Spierings et al., 2013) compared the fatigue performance of SLM and conventional cast parts and observed a lower percent of fatigue life for SLM parts at all stress ratios. While the as-built specimens revealed poor fatigue characteristics, polished samples reported improvement in fatigue life but only at low stress amplitudes. (Song et al., 2015) performed a comparative study between selective laser melted and wrought metallic specimens for fatigue life affected by the underlying micro-structure and reported an approximate 70% reduction in fatigue life for selective laser melted alloys.

(John et al., 1999) examined the fatigue crack growth rate (FCGR) characteristics of casted titanium alloy with and without laser peening. The FCGR resistance of the laser peened alloy is observed to be significantly greater than that of unpeened alloy. The increase in FCGR resistance is attributed to the superposition of applied compressive stresses on the tensile residual stresses. It is also inferred that the initiated crack remains locked if the magnitude of the applied stress is lower than the existing residual stress field.

Taking into consideration the aforementioned factors, the surface properties and residual stress distribution on the selective laser melted specimens need to be improved. Accurate design and customization of externally applied residual stress by laser shock peening might thus possibly increase the fatigue life by directing tensile residual stresses out of the critical

region. Whilst most of the work in literature is focused on studying the consequences of laser shock peening on casted alloys and hybrid AM-LSP processes, importance has to be given to the difference in fatigue properties between conventionally casted and additively manufactured metallic specimen subjected to similar laser peening treatment (which is affected by the underlying micro-structural characteristics and residual stress distribution) for foreseeable replacement in intended application. Therefore, in this thesis, the material model parameters for the casted and selective laser melted A357 aluminum alloys are initially calibrated to account for the various sources of uncertainty and subsequently treated with similar LSP configurations in order to study the induced residual stress distinction which exists as a result of differing manufacturing methodology.

The experimental set up for laser shock peening with favorable processing parameters and beam path is presented in Chapter 2. The finite element model with all the inputs needed for laser peening simulation is explained in detail in Chapter 3. Chapter 4 demonstrates the application of a probabilistic approach known as Bayesian Inference (BI) to develop a joint random field for the material model parameters. The influence of different laser peening patterns on the “candy-bar” coupon with Bayesian inference calibrated material model parameters is studied in Chapter 5. The various experimental techniques used for laser beam analysis and calibration is explained in the Appendix.

CHAPTER 2

LASER SHOCK PEENING - EXPERIMENTAL SETUP

2.1 Sample preparation

The material used in this study is an alloy of aluminum with silicon and magnesium, commonly known as the A357 grade aluminum alloy. Aluminum is the most favorable element used in the automotive and aerospace industries due to its numerous beneficial properties. Low density of aluminum has made it a promising replacement for high strength steels in the manufacturing sector. Other useful properties of aluminum include high strength to weight ratio, ductility, castability, malleability, low specific gravity and high conductivity. Among the various aluminum alloys utilized for different commercial applications, A357 in the heat treated condition is gaining popularity in the automotive and aerospace sector due to the strength enhancement provided by various heat treatment processes (Alexopoulos and Pantelakis, 2004; Zhang et al., 2002) Also, high structural durability of this alloy with good fatigue, corrosion characteristics and light weight makes it convenient for machining. (Yang et al., 2013, 2012; Kumar et al., 2007). The selective laser melted specimens used for laser peening are fabricated from a fine metal powder mainly composed of 90% aluminum, 7% silicon and 0.6% magnesium. The chemical composition of the casted A357 specimens used in this work is provided in Table 2.1. The mechanical properties of selective laser melted and casted A357 alloy is summarized in Table. 2.2.

Table 2.1. Chemical Composition of Casted A357

| Alloy element | Si | Mg | Fe | Cu | Mn | Zn | Ti |
|---------------|---------|---------|-----|-----|-----|-----|-----------|
| Weight % | 6.5-7.5 | 0.4-0.7 | 0.2 | 0.2 | 0.2 | 0.1 | 0.04-0.20 |

Table 2.2. Properties of A357 Aluminum Alloy

| Property | SLM A357 | Casted A357 |
|--------------------------------------|----------|-------------|
| 0.2% Yield Strength (<i>MPa</i>) | 293 | 241 |
| Tensile Strength (<i>MPa</i>) | 351 | 310 |
| Elongation at break (%) | 10.2 | 8 |
| Density (<i>kg/m³</i>) | 2680 | |
| Modulus of Elasticity (<i>GPa</i>) | 76 | |
| Thermal Conductivity (<i>W/mK</i>) | 160 | |
| Specific heat (<i>J/kgK</i>) | 890 | |

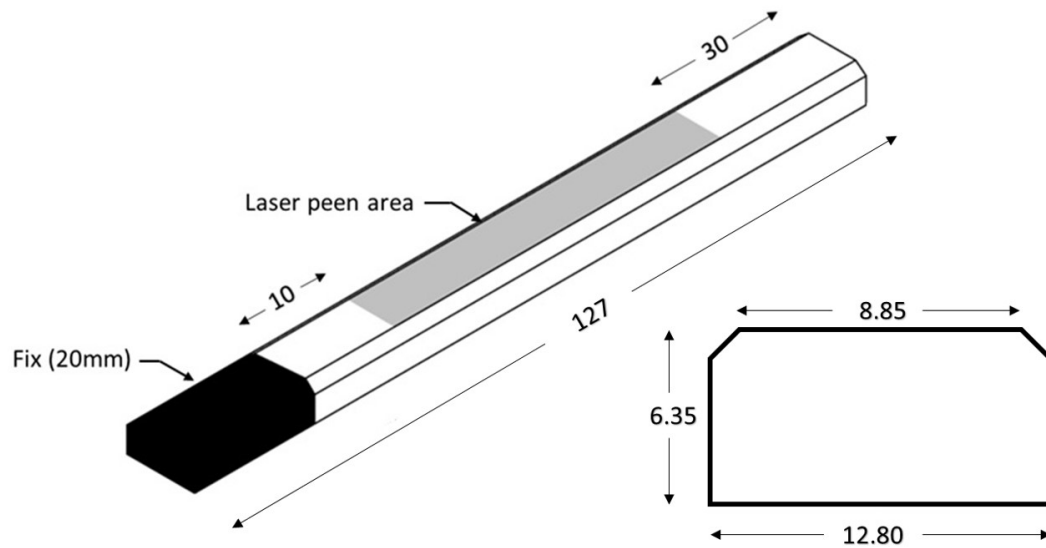


Figure 2.1. Three Point Bend Candy-bar Coupon with Cross Section (All dimensions are in *mm*)

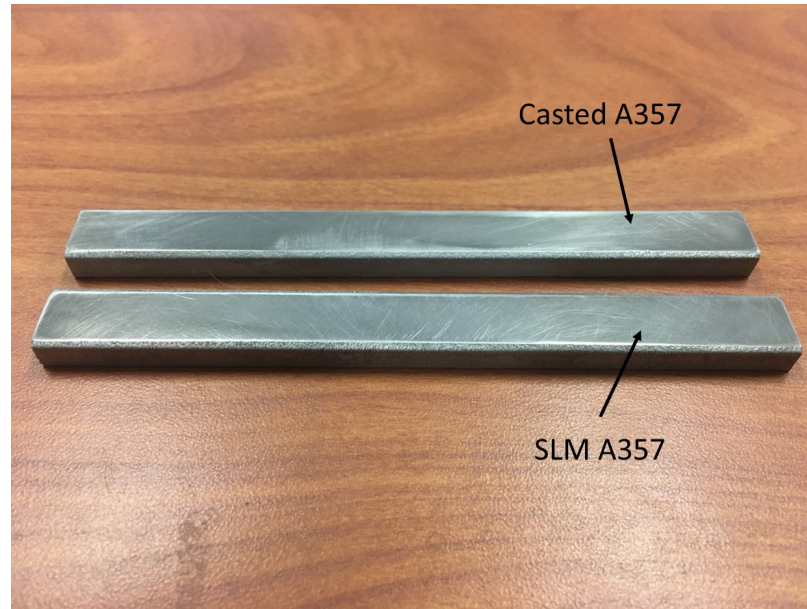


Figure 2.2. Polished SLM and Casted A357 Candy-bar Coupons

For comparing the induced residual stress field due to laser peening, specimens with a “candy-bar” cross section as shown in Fig. 2.1 is used. The candy-bar geometry is common for analyzing the coupon’s fatigue characteristics since it decreases the magnitude of stress concentration which builds up on the specimen edges as a result of repeated bending (Hasser et al., 2016; Spradlin, 2011; Luong and Hill, 2008). A 3-D CAD model with this cross section is initially designed and the specimen is then selective laser melted to obtain a solid structure. To reduce the accumulated tensile stresses in the build direction, the 3-D printed specimens are subjected to a T-6 heat treatment process. The SLM-heat treated specimens are observed to have a grainy and rough surface and hence the specimens are suitably polished using a rotary polishing machine for a good surface finish. On the other hand, the casted specimens are machined from an ingot to the required shape and size and finally polished to the same roughness as that of SLM specimens. The polished specimens used in this work are shown in Fig. 2.2. The selective laser melted specimens are analyzed for residual stresses in the

build direction prior to laser peening using X-Ray diffraction and are observed to have an approximate residual stress of -25 MPa.

2.2 Laser peening configuration

A high energy pulsed neodymium doped yttrium aluminum garnet, *i.e.*, Nd:YAG laser at 1064 nm wavelength and 10 Hz frequency is used in this work. A favorable beam path for laser peening is designed with the help of high damage threshold - laser line mirrors and collimating lenses to prevent any back reflection which might possibly damage the laser diode (refer A.1). The schematic and the actual experimental setup used in this work is illustrated in Fig. 2.3 and 2.4 respectively.

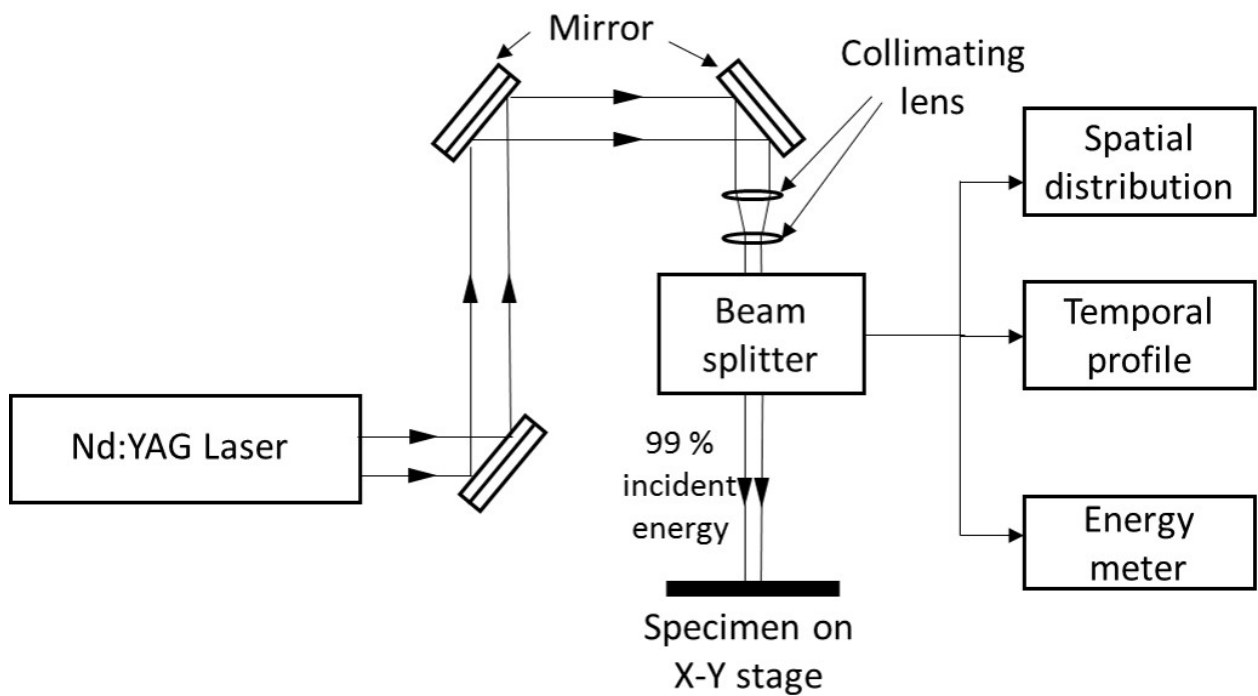


Figure 2.3. Experimental Setup - Schematic

The laser spot diameter emerging out of the laser diode is measured to be 12.7 mm which is reduced to a working diameter of 3.2 mm with a pair of collimating lenses. A relatively

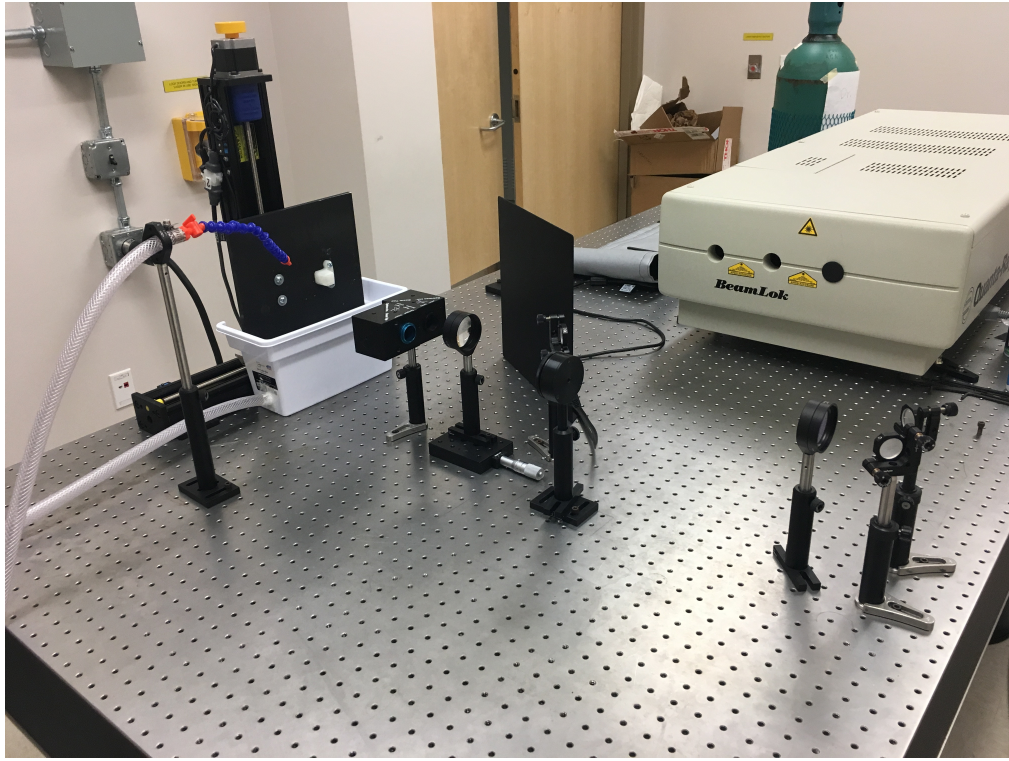


Figure 2.4. Experimental Setup - Laser lab

small amount of laser (1% of incident energy) is sampled at the beam splitter (refer A.2) to measure the laser power and to obtain the laser spatial and temporal distribution, used later in laser peening process simulation. The spatial distribution of the incident high energy laser pulse is obtained by sampling 0.01% of the laser beam at the beam splitter. The sampled beam is processed using a high speed camera and the laser energy distribution as a function of radial distance is obtained as shown in Fig. 2.5 and 2.6 respectively. The laser is observed to have a Gaussian profile with a $(1/e^2)$ Gaussian diameter of approximately 3.2 mm.

A fast photo detector (refer A.3) is connected to a high resolution oscilloscope to read the laser temporal distribution. The output of the oscilloscope which provides a plot of laser intensity versus pulse time is shown in Fig. 2.7. The laser pulse is observed to have a rise time of 26 ns with a 17 ns Full Width and Half Maximum (FWHM) pulse width.

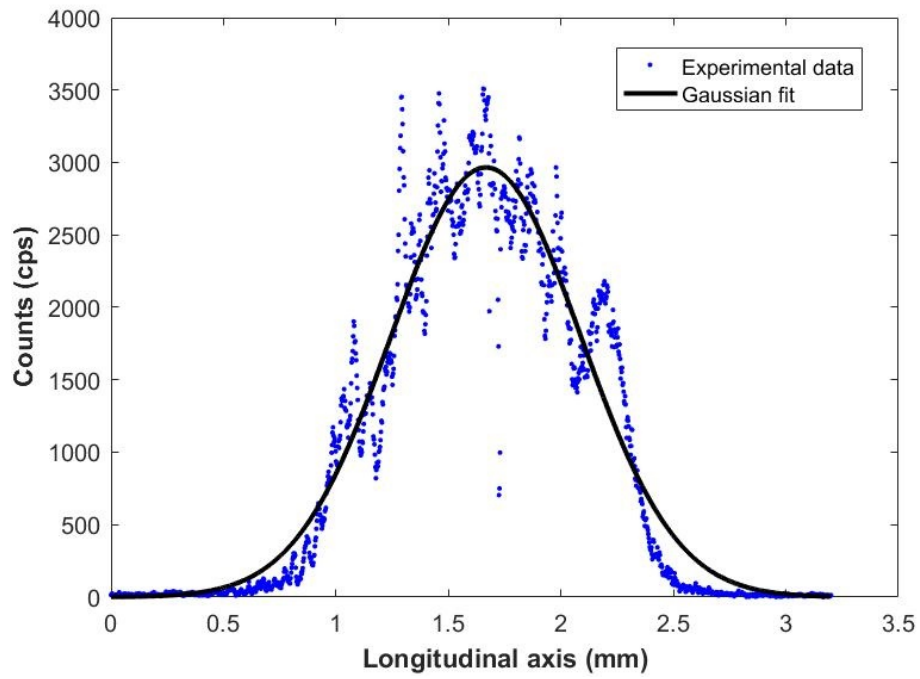


Figure 2.5. 2-D Laser Spatial Distribution

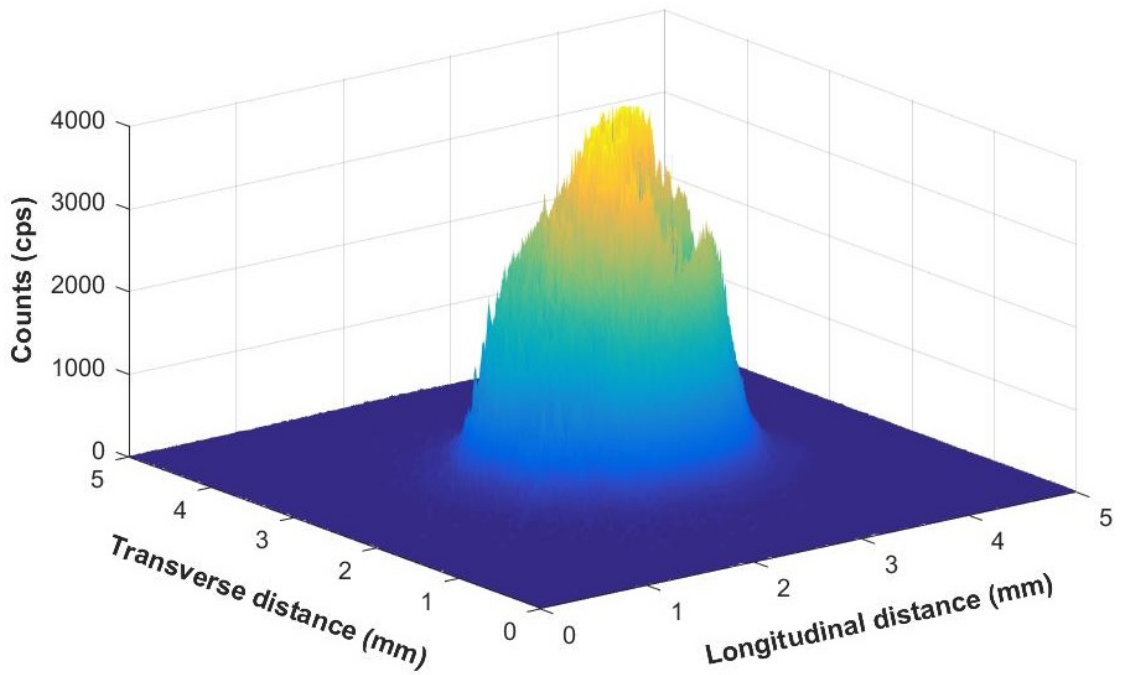


Figure 2.6. 3-D Laser Beam

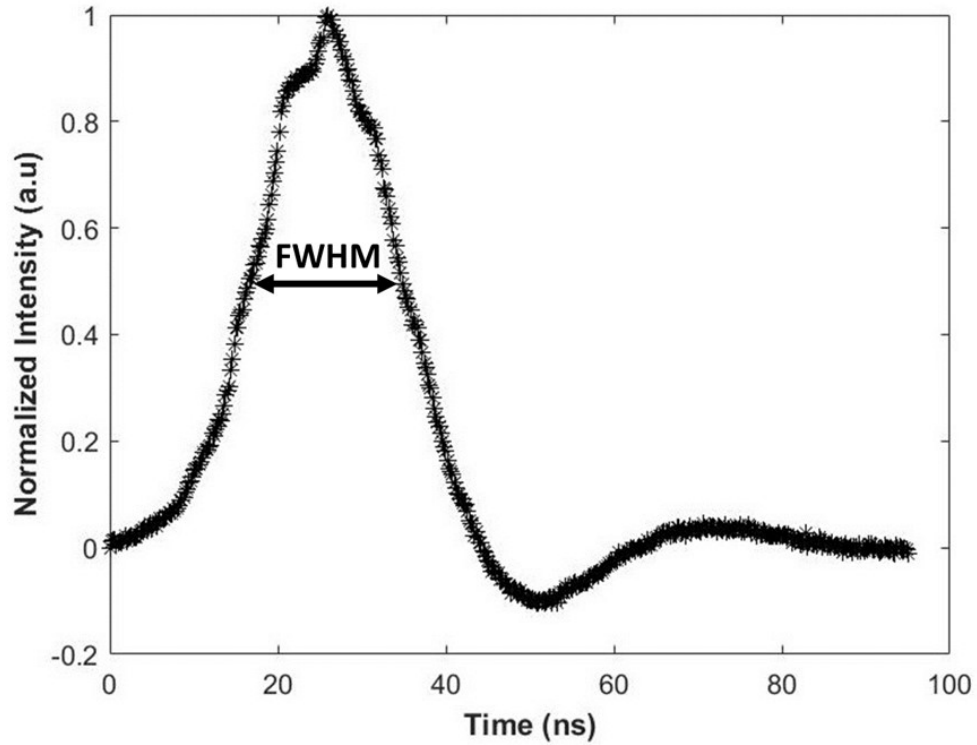


Figure 2.7. Laser Temporal Distribution

The output of the beam splitter consisting 99 % incident laser energy is directed to a servo motor operated X-Y stage. The specimen is placed on the X-Y stage with one end clamped for an approximate length of 20 *mm* as shown in Fig. 2.1. An area of 67.2 by 8 *mm* is allocated on the specimen surface to accommodate all the laser shots used in this work.

Referring to the literature, the peak power density incident on the aluminum target is assigned to 3-8 GW/cm^2 (Sathyajith et al., 2013; Wang et al., 2015; Ding and Ye, 2006). The specimen is covered with a black tape serving as the opaque overlay owing to its smooth and uniform surface finish (Sundar et al., 2012). Deionized water is used as the confining medium to enhance the resulting plasma pressure. The laser peening parameters used in this work are summarized in Table 2.3.

To ensure efficiency in predicting the residual stress field through finite element simulation of laser peening process, it is critical to determine the high strain rate material model

Table 2.3. LSP Process Parameters

| LSP parameter | Magnitude |
|------------------------|-------------------------------|
| Laser wavelength | 1064 <i>nm</i> |
| Repetition rate | 10 <i>Hz</i> |
| Pulse type | Q-Switch |
| FWHM pulse width | 17 <i>ns</i> |
| Avg. Energy | 3.5 <i>J</i> |
| Laser spot diameter | 3.2 <i>mm</i> |
| Incident power density | 4.35 <i>GW/cm²</i> |
| Opaque overlay | Black tape |
| Transparent overlay | De-ionized water |

parameters for the selective laser melted and casted specimens. For the initial material model calibration, it is common to use a relatively smaller specimen and assume symmetric boundary conditions for numerical simulations (Zhou et al., 2011, 2012). Hence, the candy-bar specimen shown in Fig. 2.1 is cut into two halves and treated with consecutive laser shots at the location shown in Fig. 2.8

For repeatability and to obtain useful statistical data, eight short specimens are initially laser peened with three completely overlapping laser shots with laser peening configuration previously shown in Table. 2.3. Following the laser peening treatment, all the specimens are analyzed for residual stress at the spot center. The statistical data of the residual stress field is used to develop a joint random field which is successively used for material model calibration, explained in detail in Chapter 4. A compressive dimple formed as a result of consecutive laser shots on the sliced candy-bar coupon is shown in Fig. 2.9.

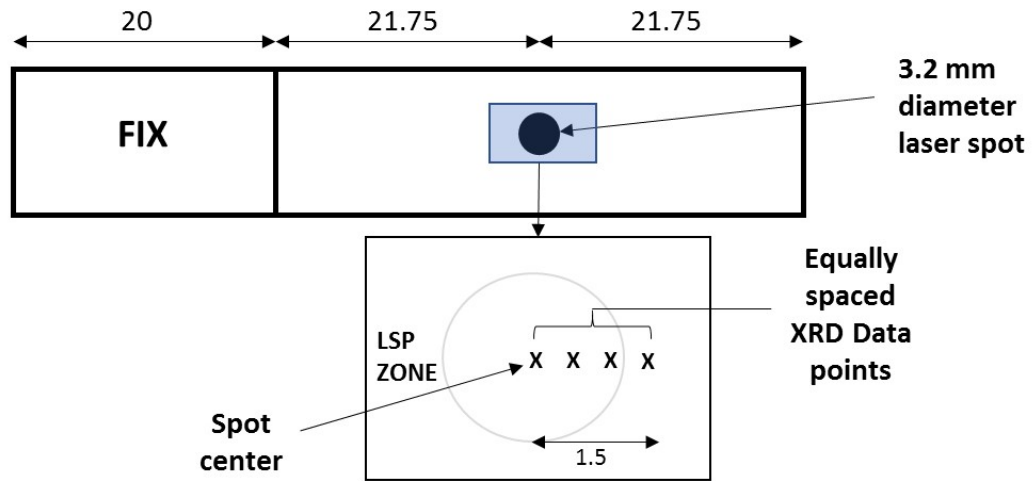


Figure 2.8. LSP Configuration for Material Model Calibration (all dimensions are in *mm*)

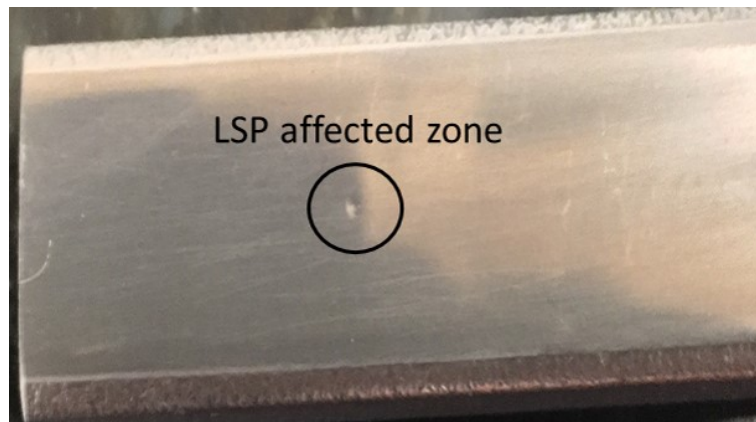


Figure 2.9. Sliced Candy-bar Specimen with LSP Affected Zone

The recorded experimental parameters used for material model calibration is summarized in Table. 2.4

Table 2.4. Recorded LSP Parameters for Material Modeling

| Specimen type | Coupon No. | Laser Energy (<i>J</i>) | Spot diameter (<i>mm</i>) |
|---------------|------------|---------------------------|-----------------------------|
| SLM A357 | 1 | 2.8 | 3.2 |
| | 2 | 2.7 | 3.2 |
| | 3 | 3.5 | 3.2 |
| | 4 | 3 | 3.2 |
| Casted A357 | 5 | 2.6 | 3.2 |
| | 6 | 3.3 | 3.2 |
| | 7 | 3.2 | 3.2 |
| | 8 | 3.1 | 3.2 |

CHAPTER 3

LASER SHOCK PEENING MODEL FOR FINITE ELEMENT SIMULATION

Ever since the initial success of finite element (FEM) techniques in predicting the residual stress distribution due to laser peening (Braisted and Brockman, 1999), researchers have subsequently tried to expedite the process simulation to address the issue of computation cost and time. Dynamic explicit analysis of the material model subjected to laser shots which is modeled as a transient pressure load followed by a static implicit relaxation analysis to settle out the model to quasi-static equilibrium is a standard baseline formulation for the LSP-FEM model. Since the baseline formulation consumes a large amount of computation time, secondary techniques to accelerate the process simulation are continuously being developed (Brockman et al., 2012; Hatamleh et al., 2017; Hasser et al., 2016).

3.1 The Single Explicit Analysis using Time Dependent Damping Method

In this work, finite element simulation of laser shock peening is modeled using the recently developed Single Explicit Analysis using Time-dependent Damping (SEATD) technique (Hasser et al., 2016). The SEATD approach, in contrast to other common techniques for LSP simulation, uses an explicit only algorithm for both shocking and variable damping periods of the LSP model rather than employing an explicit-implicit integrated technique to address the issue of computation cost and time. An extended final explicit damping period is followed after accommodating all the laser loads to de-excite the LSP-FEM model to quasi-static equilibrium. It is recently shown that the use of variable damping for laser peening simulation results in significant reduction of computation time without compromising the accuracy of predicted surface residual stresses (Hasser et al., 2016). Also, a systematic method for modeling an efficient variable damping profile using modal analysis for different laser peening conditions is recently developed (Hatamleh et al., 2017). The flowchart describing all the inputs needed for the SEATD technique is provided in Fig. 3.1.

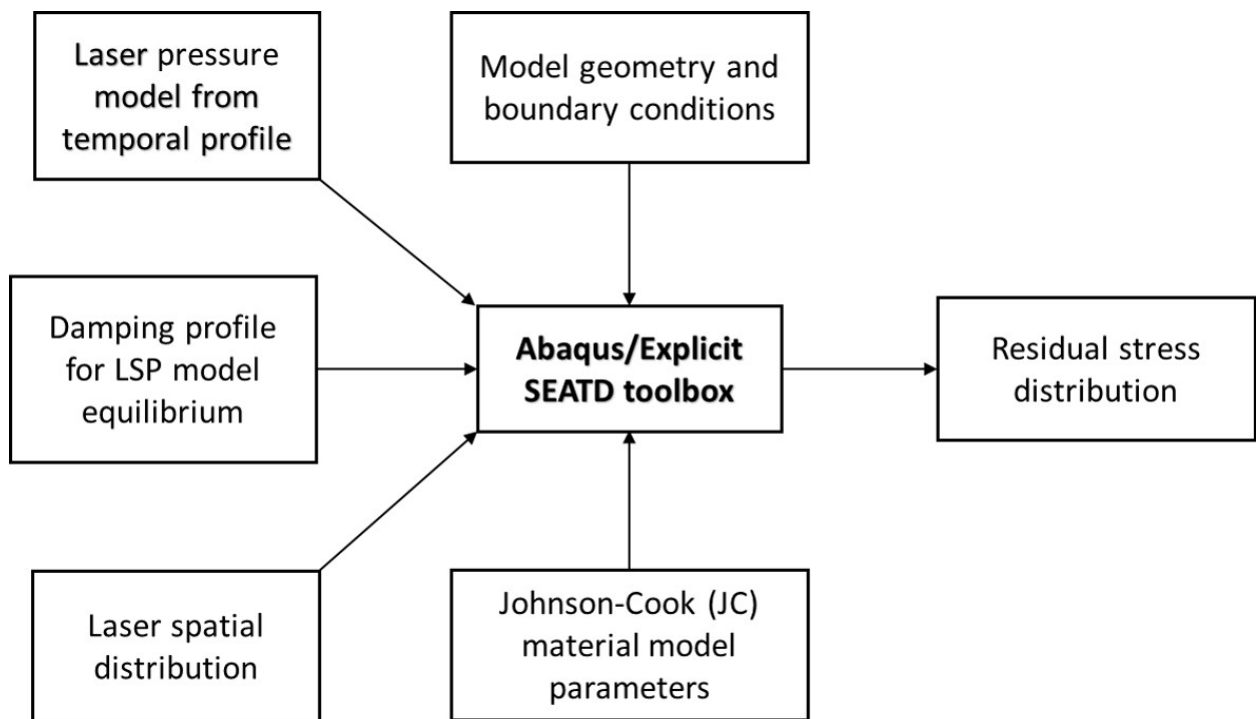


Figure 3.1. Inputs for the SEATD Technique

The commercially available FEM package, *Abaqus/Explicit* (Hibbitt et al., 2001) is used for all numerical simulations. In this work, the formulation of SEATD technique involves an assignment of an initial loading period of $2 \mu s$ to capture all the plastic interactions due to laser shocking. This is followed by a variable damping period of $8 \mu s$ to settle the model for the application of next LSP-FEM load. After accommodating all the transient loads, the LSP-FEM model is subjected to an extended final damping period of $200 \mu s$ to attain the quasi-static equilibrium state.

The sliced specimen with a candy-bar cross section previously shown in Fig. 2.8 is used for the initial material model calibration with one end subjected to “*Encastre*” boundary condition. The Gaussian distribution obtained from the high speed camera shown in Fig. 2.5 is used as the laser spatial profile. For simplicity, the variable damping profile used in

previous work is currently used to de-excite the LSP model between consecutive laser shots (Hasser et al., 2016).

Considering the time consuming process of LSP simulation and the need for performing multiple simulations for surrogate modeling (discussed in Chapter 4), a suitable mesh is designed to expedite simulations with a reasonable residual stress accuracy. Hence, 8,90,590 coupled temperature-displacement and reduced integration elements (C3D8RT) available in *Abaqus/Explicit* with a mesh spacing of $60 \mu m$ at spot location and $300 \mu m$ elsewhere is used for the initial material model calibration with the LSP configuration previously shown in Fig. 2.8. Through experience, this mesh spacing is just enough to accommodate the equivalent plastic strain whilst ensuring stability. Since the opaque overlay absorbs a higher fraction of thermal energy in generating the high pressure plasma, the residual thermal energy incident on the specimen is negligible and hence ignored. Although the SEATD method requires the use of coupled temperature-displacement elements, the thermal effects are ignored by assuming ambient conditions ($T = T_0$).

3.1.1 Plasma Pressure Model

The laser pressure model is one of the most influential factors affecting the residual stress distribution due to laser peening. A variety of pressure models are used in the literature for laser shock peening simulation. A triangular ramp to depict the Gaussian laser pulse with a linear increase in pressure upto the peak pressure followed by a steady decrease is quite common (Braisted and Brockman, 1999; Kim et al., 2013). Velocity Interferometer System for Any Reflector (VISAR) doppler velocimetry is also used to obtain the back free surface velocity (u_F) which is indeed a function of the plasma pressure (Peyre et al., 2003, 2007; Hfaiedh et al., 2015). While the triangular ramp model is easy to implement, it does not give a reliable residual stress prediction (Braisted and Brockman, 1999). Also, to avoid the additional expense on experimental techniques in plasma pressure modeling without

affecting the residual stress accuracy, a 1-D hydrodynamic plasma pressure model developed by (Fabbro et al., 1990) is used.

Per Fabbro, in a water-confined regime, the incident laser energy on the substrate is used by the plasma for ionization and thermal energy augmentation resulting in expansion of relatively larger volume of plasma in water. The transient plasma pressure $P(t)$ (GPa) during the heating phase is a function of the incident laser intensity $I(t)$ (GW/cm²), the plasma thickness $L(t)$ (cm) and the reduced shock impedance Z (g/cm²s) as shown in Eq. 3.1, 3.2 and 3.3.

$$\frac{1}{Z} = \left(\frac{1}{Z_1} + \frac{1}{Z_2} \right) \quad (3.1)$$

$$\frac{dL(t)}{dt} = \frac{P(t)}{Z} \quad (3.2)$$

$$\frac{dL(t)}{dt} = P(t) \frac{dL(t)}{dt} + \frac{3}{2\alpha} \frac{d}{dt} [P(t)L(t)] \quad (3.3)$$

where Z_1, Z_2 (g/cm²s) refers to the shock impedance of water and aluminum respectively and α is the fraction of internal energy converted to thermal energy.

Coupling Eq. 3.2 and 3.3 results in a non-linear second order ordinary differential equation (ODE) as given in Eq. 3.4

$$\frac{d^2 L(t)}{dt^2} = \frac{I(t)}{c_1 L(t)} - \frac{c_1 + c_2}{c_1} \left(\frac{dL(t)}{dt} \right)^2 \frac{1}{L(t)}$$

where $c_1 = \frac{3Z}{4\alpha}$ and $c_2 = \frac{Z}{2}$ (3.4)

Subsequent to the heating phase, *i.e.*, past the full width and half maximum (FWHM) of laser temporal distribution (τ), the existing plasma pressure tends to decrease with time due

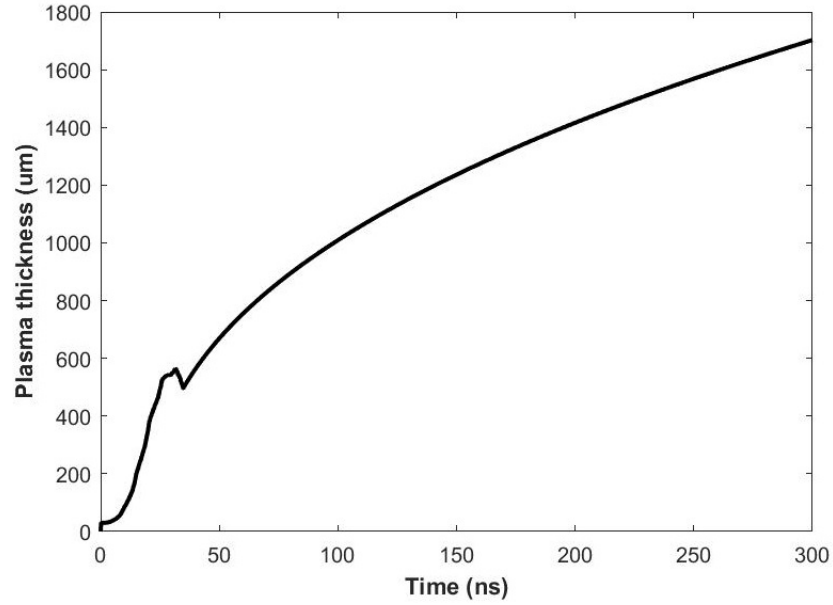


Figure 3.2. Plasma Thickness

to adiabatic cooling as given in Eq. 3.5. The parametric constants used for plasma pressure modeling in this work are summarized in Table 3.1.

$$P(t) = P(\tau) \left(\frac{L(\tau)}{L(t)} \right)^\gamma \quad (3.5)$$

where γ is the adiabatic constant

Table 3.1. Parametric Constants for Plasma Pressure Modeling

| Model parameter | Magnitude |
|------------------------------|----------------------------------|
| Energy ratio (α) | 0.25 |
| Water impedance (Z_1) | $1.65e5 \text{ gm/cm}^2\text{s}$ |
| Aluminum impedance (Z_2) | $2.75e6 \text{ gm/cm}^2\text{s}$ |

Numerical solution of the coupled Eq. 3.4 - 3.5 ODE gives the required plasma pressure model. While modeling the plasma pressure, it is ensured that the peak pressure is around 2-

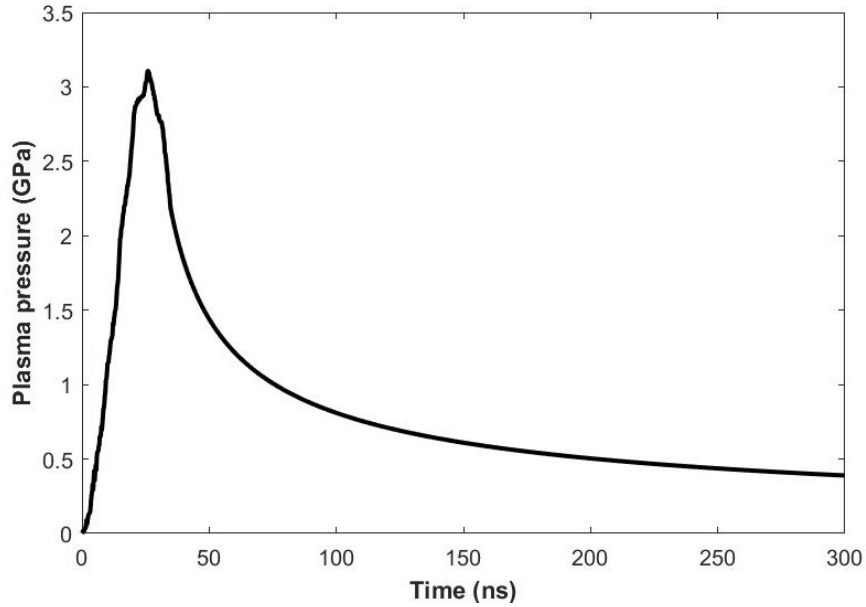


Figure 3.3. Plasma Pressure

2.5 times the Hugoniot Elastic Limit (HEL) to accommodate all the resulting plastic strains due to the compressive stress field. The HEL as a function of dynamic yield strength (σ_d) is given in Eq. 3.6.

$$HEL = \frac{(1 - \nu)\sigma_d}{(1 - 2\nu)} \quad (3.6)$$

where ν is the Poisson's ratio

Using the temporal distribution obtained from the fast photo detector (Fig. 2.7), the plasma thickness and plasma pressure history modeled using the aforementioned formulation is shown in Fig. 3.2 and 3.3 respectively.

3.1.2 Material model

Since the modeled transient pressure pulse results in a rate dependent inelastic behavior of the LSP model, a viscoplastic material model to determine the flow stress during plastic deformation is coupled with the linear isotropic elasticity model to render the elasto-plastic

behavior of the solid. Of all the available flow stress models in the literature, Johnson-Cook (JC) material model is employed in this work due to its ability to account for the high strain rates reported in LSP (10^6 s^{-1}) along with its ease of application (Amarchinta et al., 2010; Zhou et al., 2012; Peyre et al., 2007). The flow stress as a function of equivalent plastic strain (ϵ_p), the plastic strain rate ($\dot{\epsilon}_p$) and the working temperature (T) as accommodated by the Johnson-Cook material model is given in Eq. 3.7.

$$\sigma_y(\epsilon_p, \dot{\epsilon}_p, T) = \left[A + B(\epsilon_p)^n \right] \left[1 + C \ln \left(\frac{\dot{\epsilon}_p}{\dot{\epsilon}} \right) \right] \left[1 - (T^*)^m \right]$$

$$\text{where } T^* = \frac{T - T_0}{T_m - T_0} \quad (3.7)$$

Here, A, B, C, n, m are the Johnson-Cook parameters, $\dot{\epsilon}$ is the quasi-static strain rate, T_m is the melt temperature and T_0 is the ambient temperature.

A set of published Johnson-Cook parameters for A357 aluminum alloy by (Gupta et al., 2014) shown in Table. 3.2 is used in this work, as an initial dataset. Since these published parameters are just an approximate and depict the material behavior at a low strain rate of 5000 s^{-1} in contrast to the actual laser peening conditions, a set of high strain rate Johnson-Cook parameters is developed in this work based on the experimental residual stress using Bayesian Inference.

Table 3.2. Johnson-Cook Parameters for A357 Alloy adapted from (Gupta et al., 2014)

| JC parameter | Value |
|--|---------|
| Yield Strength (A) | 313 MPa |
| Strain hardening parameter(B) | 184 MPa |
| Strain hardening exponent (n) | 0.27 |
| Strain rate sensitivity (C) | 0.014 |
| Temperature exponent (m) | 1.55 |
| Melt temperature (T_m) | 557°C |
| Reference strain rate ($\dot{\epsilon}$) | 1/s |

CHAPTER 4

UNCERTAINTY QUANTIFICATION OF MATERIAL MODEL USING BAYESIAN INFERENCE

4.1 Introduction

The sources of error while performing laser shock peening are high due to the numerous process variables involved. Published articles claim that the fatigue lives of laser peened components with similar processing conditions are not consistent (Clauer et al., 1981; Clauer, 1996). While the existing material model calibration techniques for laser peening simulation in the literature deal with deterministic parameters (Amarchinta et al., 2010; Zhou et al., 2012) consideration of various uncertainties involved in the laser peening process is critical to optimize the process for the most beneficial stress field. A joint random field for the material model parameters is therefore developed using a common probabilistic approach known as Bayesian Inference which can be coupled with any probabilistic optimization technique for laser shock peening.

Bayesian Inference (BI) is a probabilistic tool commonly used to quantify the uncertainties associated with an available dataset. The goal of using this technique is to determine the probability of observing a particular residual stress which is a function of several correlated random variables (Nelson et al., 2014; Park et al., 2010). The process relies on the principle of Bayes' theorem which predicts the probability of an event to occur according to Eq. 4.1.

$$P(A|B) = \frac{P(B|A)P(A)}{P(B)} \quad (4.1)$$

In Eq. 4.1, $P(A|B)$ is the posterior probability of A given B , $P(B|A)$ is the likelihood of B given A , $P(A)$ is the prior probability of A and $P(B)$ is the total probability of B .

4.2 Probabilistic Distribution of Johnson-Cook parameters

In this work, since the Johnson-Cook model parameters obtained from the literature do not depict the actual physics of laser peening and also to account for various intrinsic errors in experiments, measurements, the material model and the material itself, a joint probability mass function (PMF) for the correlated Johnson-Cook parameters, namely, the yield stress (A), the strain hardening parameter (B), the strain hardening exponent (n) and the strain rate sensitivity parameter (C) is developed such that it predicts the pre-determined experimental residual stress yet accounts for the estimated experimental and other errors. The advantage of using Bayesian Inference is that the material model parameters are calibrated with each Bayesian update with respect to the experimental residual stress while considering the sources of mutual uncertainty. The modified version of Bayes' theorem reflecting this problem statement is shown in Eq. 4.2.

$$P(A, B, n, C | \sigma_{res} = \sigma_{exp}) = \frac{[P(\sigma_{res} = \sigma_{exp} | A, B, n, C)] * [P(A, B, n, C)]}{P(\sigma_{res} = \sigma_{exp})} \quad (4.2)$$

In Eq. 4.2, $P(A, B, n, C | \sigma_{res} = \sigma_{exp})$ refers to the posterior probability of obtaining a joint PMF for the Johnson-Cook parameters, given the experimental residual stress (σ_{exp}), $P(A, B, n, C)$ is the prior probability (belief) that the Johnson-Cook parameters follow a certain joint PMF, $P(\sigma_{res} = \sigma_{exp} | A, B, n, C)$ is the likelihood function which refers to the probability of a particular combination of the Johnson-Cook parameters to yield the experimental residual stress and $P(\sigma_{res} = \sigma_{exp})$ refers to the total probability of the predicted residual stress agreeing with the experimental residual stress for all combinations of Johnson-Cook parameters.

For the Bayesian updating process, the variables are initially discretized into N uniformly distributed samples resulting in N^t Bayesian grid points in the design hyperspace, t refers to the number of random variables. Note that the term “random variables” refer to the

dispersion of Johnson-Cook parameters for the joint PMF computation in Bayesian Inference whereas design variables or “design points” refer to the Latin Hypercube Sampled (LHS) points for surrogate modeling. The PMF of random variables and design points can hence be different. The residual stress at each Bayesian grid point is calculated which is successively used in Bayesian iterations. For simplicity and to ensure computational efficiency, initially, the residual stress at only one node on the LSP-FEM model is consistently predicted across all the Bayesian grid points. The prior probability is initially assumed to be a uniform joint distribution of Johnson-Cook parameters given by N^{-t} . The upper and lower bounds for the initial uniform distribution is defined to accommodate a wide range of random variables. The possibility of obtaining multiple JC parameter sets reflecting the experimental residual stress is thus highly likely due to the widely dispersed prior joint PMF. However, this issue is accounted for by incorporating a suitable likelihood function explained later in Section 4.2.2. The prior probability and the likelihood function used with the total probability of the experimental residual stress throughout the design hyperspace facilitates the posterior joint PMF determination for the first iteration. For subsequent updates, the posterior PMF of the previous iteration is considered to be the prior PMF of the current iteration and the process is repeated until convergence. This process is depicted in a flow chart in Fig. 4.1.

4.2.1 Surrogate Modeling

Since each numerical simulation results in significant consumption of computation time (6 hours with 5 CPUs), an approximate for the LSP-FEM model is developed to calculate the residual stress at each Bayesian grid point. Due to its retained fidelity over a large domain in the design hyperspace, a non-linear regression based kriging surrogate model is developed (Forrester et al., 2008; Forrester and Keane, 2009). To develop an efficient and reliable surrogate model, a specified minimum set of design points are initially sampled using the rank correlated LHS plan such that all the sampled points are evenly distributed in the domain

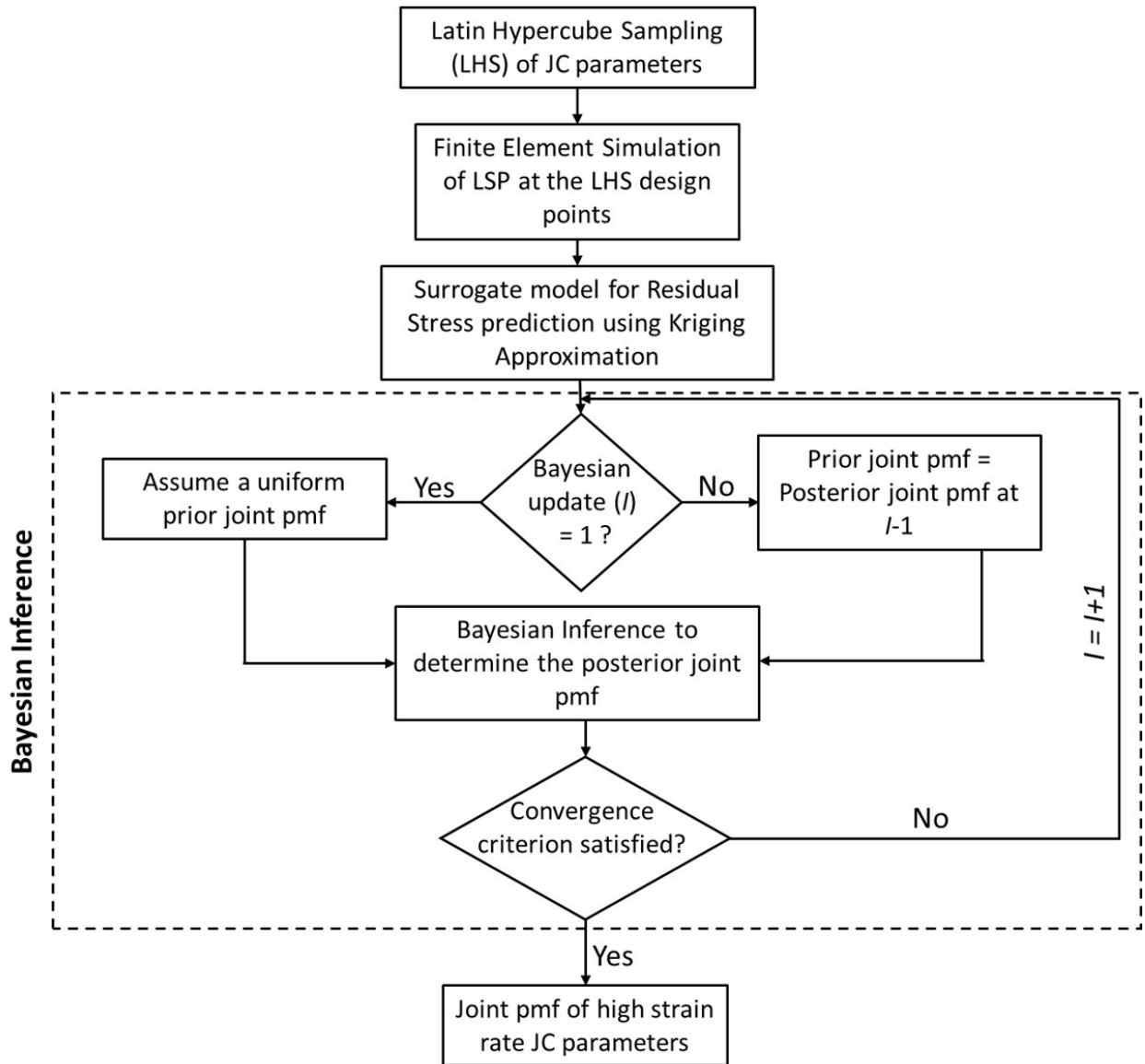


Figure 4.1. Bayesian Inference of JC parameters

without any repetition. The Johnson-Cook parameters previously established in Table 4.2 are thus considered the mean of design points and a suitable coefficient of variation is assumed for parameter dispersion through the mean for the initial LHS. Numerical simulation of laser peening process is carried out at the design points and the residual stress at the node corresponding to the spot center is recorded. A surrogate model for the residual stress is then developed based on the recorded data.

4.2.2 Likelihood function

In this work, a Gaussian type kernel density probability mass function given in Eq. 4.3 is assumed to serve as the likelihood function (Nelson et al., 2014)

$$P(\sigma_{res}|A, B, n, C) = \exp\left(\frac{-(\sigma_{res} - \sigma_{exp})^2}{2h^2}\right) \quad (4.3)$$

in which σ_{res} denotes the predicted residual stress, σ_{exp} is the experimental residual stress and h is a free or the smoothing parameter more often known as the “standard error”. The likelihood function would result in a non-zero PMF if the predicted residual stress with a particular set of JC constants is in the neighborhood of experimental residual stress. Else, the user-defined standard error (h) would penalize the predicted stress and return a near-zero PMF. The selection of standard error is very critical to account for all the sources of uncertainty.

For simplicity, the experimental data is often assumed to follow a Gaussian distribution and the corresponding asymptotic mean squared error (AMSE) between the assumed and kernel distribution is optimized. The published optimal standard error as a function of the Gaussian distributed experimental data (Turlach et al., 1993) is given in Eq. 4.4

$$h = 1.06\sigma q^{-\frac{1}{5}} \quad (4.4)$$

In the above equation, σ is the standard deviation of the experimental data and q denotes the number of experimental data points.

4.2.3 Posterior Probability

The posterior probability, *i.e.*, the joint PMF of Johnson-Cook model parameters, given the experimental residual stress is determined using the prior probability, total probability and likelihood function as explained previously. A concise expression for the first posterior probability calculation used in this work is given in Eq. 4.5

$$P_I(A_i, B_j, n_k, C_l | \sigma_{res}) = \left[\exp\left(\frac{-(\sigma_{res}^{i,j,k,l} - \sigma_{exp})^2}{2h^2}\right) N^{-t} \right]_* \left[\sum_{i=1}^N \sum_{j=1}^N \sum_{k=1}^N \sum_{l=1}^N \exp\left(\frac{-(\sigma_{res}^{i,j,k,l} - \sigma_{exp})^2}{2h^2}\right) N^{-t} \right]^{-1} \quad (4.5)$$

In the above equation, I is the index of Bayesian iteration and N^{-t} represents the uniform distribution of Johnson-Cook parameters for prior probability in the first Bayesian update. For subsequent iterations ($I > 1$), the term N^{-t} is replaced by $P_{I-1}(A_i, B_j, n_k, C_l | \sigma_{res})$, *i.e.*, the posterior probability of the previous iteration. The process is then iterated upon convergence.

4.3 Extending Bayesian Inference across Multiple Experimental Dimensions

The efficiency of Bayesian inference and the degree of accuracy of the obtained joint PMF for the Johnson-Cook parameters is highly dependent on the number of design points in the surrogate model and the number of uniform grid points (N) across each parameter. Keeping the number of design points a mere constant, a coarser N would result in fewer Bayesian grid points and a finer N would result in higher grid points thereby predicting a more accurate solution. However, while using a finer N , the possibility of multiple grid points to predict the given experimental residual stress is highly likely.

In addition, while the experimental residual stress distribution varies across the longitudinal direction, it is expected that the FEM simulation with the Bayesian inference calibrated

Johnson-Cook parameters give a similar distribution. However, when using a fine grid mesh, the possibility of predicting the experimental residual stress at a different location with consistent Johnson-Cook parameters is highly unlikely with independent Bayesian iterations across the FEM nodes.

Therefore, the likelihood function formulated in Eq. 4.3 is modified with an aim to predict a reliable set of Johnson-Cook parameters which further gives a reasonable residual stress field.

For this reason, the terms σ_{res} , σ_{exp} and h , which initially was a scalar is now a vector containing residual stress values at different locations. The posterior probability with the modified likelihood function is given in Eq. 4.6a and 4.6b respectively.

For $I = 1$

$$P_I(A_i, B_j, n_k, C_l | \sigma_{res}^{\vec{}}) = \left[\exp\left(\frac{-|\sigma_{res}^{\vec{}}{}^{i,j,k,l} - \sigma_{exp}^{\vec{}}|^2}{2|\vec{h}|^2}\right) N^{-t} \right] * \left[\sum_{i=1}^N \sum_{j=1}^N \sum_{k=1}^N \sum_{l=1}^N \exp\left(\frac{-|\sigma_{res}^{\vec{}}{}^{i,j,k,l} - \sigma_{exp}^{\vec{}}|^2}{2|\vec{h}|^2}\right) N^{-t} \right]^{-1} \quad (4.6a)$$

For $I > 1$

$$P_I(A_i, B_j, n_k, C_l | \sigma_{res}^{\vec{}}) = \left[\exp\left(\frac{-|\sigma_{res}^{\vec{}}{}^{i,j,k,l} - \sigma_{exp}^{\vec{}}|^2}{2|\vec{h}|^2}\right) P_{I-1}(A_i, B_j, n_k, C_l | \sigma_{res}^{\vec{}}) \right] * \left[\sum_{i=1}^N \sum_{j=1}^N \sum_{k=1}^N \sum_{l=1}^N \exp\left(\frac{-|\sigma_{res}^{\vec{}}{}^{i,j,k,l} - \sigma_{exp}^{\vec{}}|^2}{2|\vec{h}|^2}\right) P_{I-1}(A_i, B_j, n_k, C_l | \sigma_{res}^{\vec{}}) \right]^{-1} \quad (4.6b)$$

In the above equations, $-|\sigma_{res}^{\vec{}}{}^{i,j,k,l} - \sigma_{exp}^{\vec{}}|$ represents the norm of the difference between the multidimensional predicted and experimental residual stress vector.

4.4 Material Model Calibration of Casted and SLM A357

To demonstrate the process of Bayesian Inference, a set of test data for the residual stress field averaged at 4 spatial nodes previously shown in Fig. 2.8 is assumed for the SLM

and casted A357 specimens as shown in Table. 4.1. The corresponding residual stresses are labeled as *RS-0*, *RS-0.5*, *RS-1* and *RS-1.5* as per the longitudinal distance from spot center.

Table 4.1. Assumed Test Data for Experimental Residual Stress (for BI Demonstration)

| XRD-Location (mm) | SLM A357 RS (MPa) | Casted A357 RS (MPa) |
|--------------------------|--------------------------|-----------------------------|
| 0 (<i>RS-0</i>) | -176 | -287 |
| 0.5 (<i>RS-0.5</i>) | -130 | -148 |
| 1 (<i>RS-1</i>) | -68 | -87 |
| 1.5 (<i>RS-1.5</i>) | -34 | -47 |

As per the flow chart given in Fig. 4.1, the process of Bayesian inference begins with the formulation of a surrogate model to predict the surface residual stress distribution on the sliced candybar specimen subjected to three consecutive laser shots. For a reliable surrogate model, the definition of mean and coefficient of variation for the design points are critical. The Johnson-Cook parameters for A357 alloy given in Table. 3.2 is considered the mean for the SLM and casted alloys. A tolerance level of 40% is initially assumed for a wide dispersion of design points. With these statistical data, a set of 50 design points are obtained based on the LHS plan such that there are no repetitions. Finite element simulation of LSP with the LHS parameters for *A*, *B*, *n* and *C* results in 50 different residual stress values which are fed into the surrogate model. The LHS domain for each Johnson-Cook parameter is given in Table. 4.2

For the Bayesian Inference process, each parameter is discretized into 95 grid points thereby giving rise to $95^4 = 8 * 10^7$ Bayesian grid points. The surrogate model is iteratively used to obtain a reasonable residual stress prediction across all the Bayesian grid points. The prior PMF of the residual stress at the spot center before Bayesian inference is given in Fig.

Table 4.2. LHS Domain

| JC parameter | Lower bound | Upper bound |
|--------------|-------------|-------------|
| A (MPa) | 187.8 | 438.2 |
| B (MPa) | 110.4 | 257.6 |
| n | 0.162 | 0.378 |
| C | 0.0084 | 0.0196 |

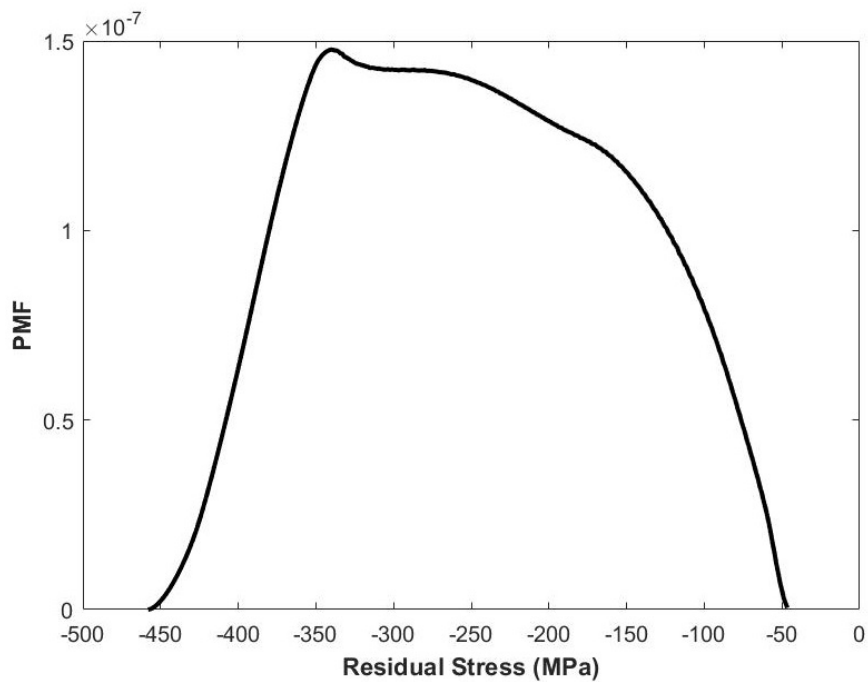


Figure 4.2. Residual Stress - Prior PMF

4.2. Note that while this curve on the plot is continuous, it indeed represents a PMF not a probability density function (PDF), since it represents the probability of discrete residual stress values (hence the sum of PMF probabilities is unity, rather than the integral of the curve being unity). The same is true for subsequent PMF plots in this section.

It is noticed from Fig. 4.2 that the prior PMF of residual stress is relatively flat with an upper and lower bound of -50 MPa and -450 MPa respectively. The peak probability as seen in Fig. 4.2 is 1.48×10^{-7} . While the range of prior PMF is wide resulting in a higher and almost equal probability for unrealistic residual stresses, it is expected to obtain a central-tendency distribution with the mean experimental residual stress while performing successive Bayesian iterations. Also, the prior PMF for the residual stress in Fig. 4.2 is consistent with both SLM and casted A357 specimens due to an assumption of similar initial parameter dispersion. The prior probability for the first iteration is $1/N^t = 1.23 \times 10^{-8}$. For the likelihood function given in Eq. 4.3, the calculation of standard error h is critical. Hence, the statistical data, *i.e.*, the mean (μ_{exp}) and standard deviation (σ) of experimental residual stress are calculated for the SLM and casted specimens.

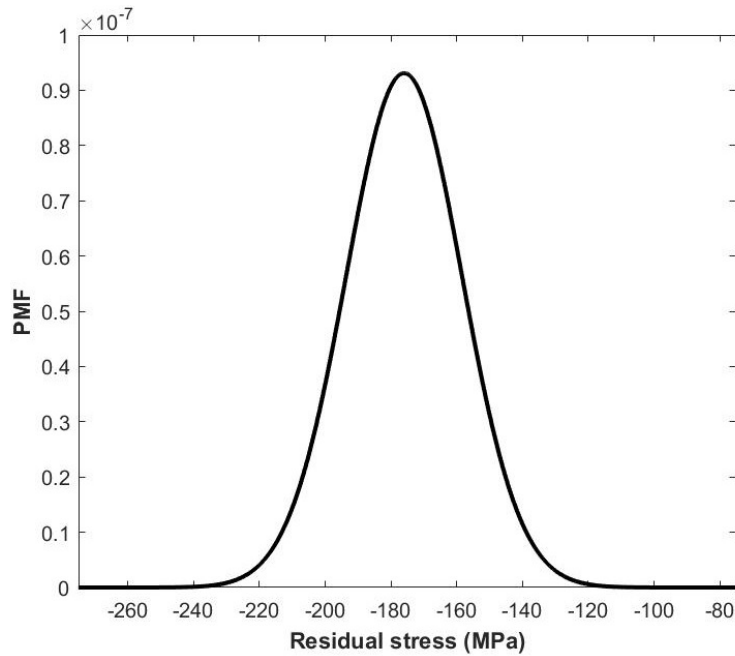


Figure 4.3. SLM Residual Stress ($RS-0$) - Iteration 1

Initially, for the SLM specimens, the mean and standard deviation of the experimentally determined residual stress at the spot center ($RS-0$) are assumed to be -176 MPa and -22 MPa respectively. In this work, the mean (μ_{exp}) is considered to be the actual residual

stress which is to be predicted by the calibrated Johnson-Cook parameters. Assuming the experimental data points to contain normally distributed error, using Eq. 4.4, the value of standard error results in -17.6MPa . Having calculated all the Bayesian parameters, the first iteration of the Bayesian Inference process results in the distribution given in Fig. 4.3. It is evident from Fig. 4.3 that the current iteration has resulted in the predicted residual stress being dispersed around the experimental residual stress which is indeed the mean of the current distribution.

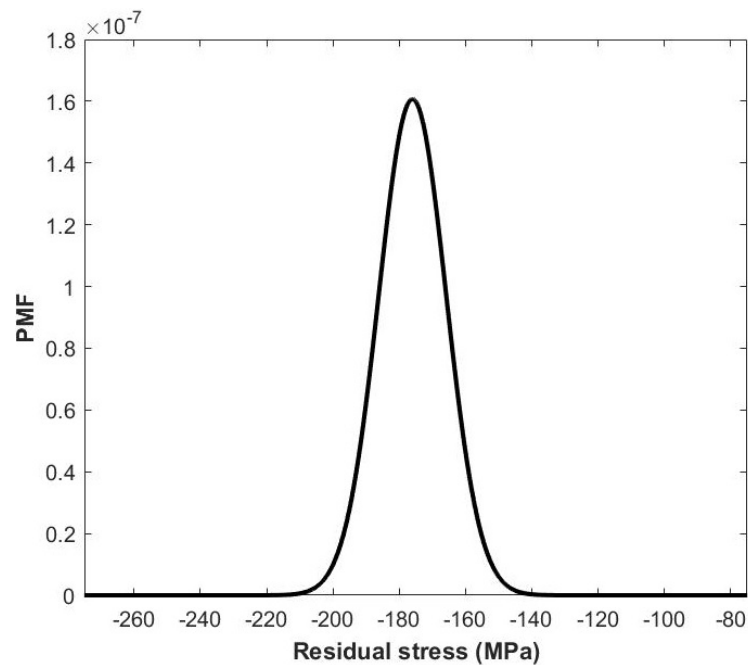


Figure 4.4. SLM Residual Stress ($RS-\theta$) - Iteration 3

Fig. 4.4 depicts the residual stress PMF after the final iteration, *i.e.*, Iteration-3. It is seen that the peak probability is now increased from $9.3 * 10^{-8}$ to $1.6 * 10^{-7}$. Also, on comparing Fig. 4.3 and 4.4, a reduced dispersion for the third iteration is observed. This is due to the fact that the current joint posterior PMF is calculated based on the prior posterior PMF.

Similar process is repeated for the casted A357 specimens with an assumed μ_{exp} , σ and h of -287MPa , -35.73MPa and -28.7MPa respectively. The Johnson-Cook parameters

Table 4.3. Calibrated Johnson-Cook Parameters for $RS-0$

| JC parameter | SLM (RS-0) | Casted (RS-0) |
|--------------|------------|---------------|
| A (MPa) | 286.36 | 345 |
| B (MPa) | 173.03 | 180.86 |
| n | 0.3458 | 0.3711 |
| C | 0.0104 | 0.0185 |

which predict the actual residual stress at the spot center is obtained from the 4-D joint PMF of A , B , n and C . The calibrated Johnson-Cook parameters for predicting the residual stress at spot center ($RS - 0$) is given in Table. 4.3.

4.4.1 Multidimensional Extension

Since a finer grid mesh (95 grid points for A , B , n and C) is used in the previous section for material model calibration at the spot center, the possibility of the Bayesian inferred Johnson-Cook parameters to predict the actual residual stress at other longitudinal nodes is highly unlikely as previously explained in Section 4.3. To study this, the surrogate model for residual stress is redesigned for the nodes $RS - 0.5$, $RS - 1$ and $RS - 1.5$ respectively. Table 4.4 gives the output of Bayesian Inference for the individual spatial nodes.

It is noted from Table. 4.4 that the Johnson-Cook parameters previously predicted in Table. 4.3 is not consistent with different spatial nodes in the longitudinal direction. The residual stresses predicted by the Johnson-Cook parameters in Tables. 4.3 and 4.4 at different spatial nodes for the SLM and casted specimens are compared in Fig. 4.5 and 4.6 respectively.

Table 4.4. Bayesian Inference Output for *RS-0.5*, *RS-1* and *RS-1.5*

| Bayesian Inferred JC Parameter | SLM | | | Casted | | |
|--------------------------------|--------------|--------|--------|--------------|--------|--------|
| | Spatial node | | | Spatial node | | |
| | RS-0.5 | RS-1 | RS-1.5 | RS-0.5 | RS-1 | RS-1.5 |
| A (MPa) | 190.47 | 246.40 | 238.41 | 273.04 | 190.47 | 193.12 |
| B (MPa) | 243.50 | 248.20 | 180.86 | 110.4 | 157.37 | 124.5 |
| n | 0.1712 | 0.2447 | 0.2080 | 0.2677 | 0.1666 | 0.2838 |
| C | 0.0129 | 0.0116 | 0.0098 | 0.0084 | 0.0108 | 0.0130 |

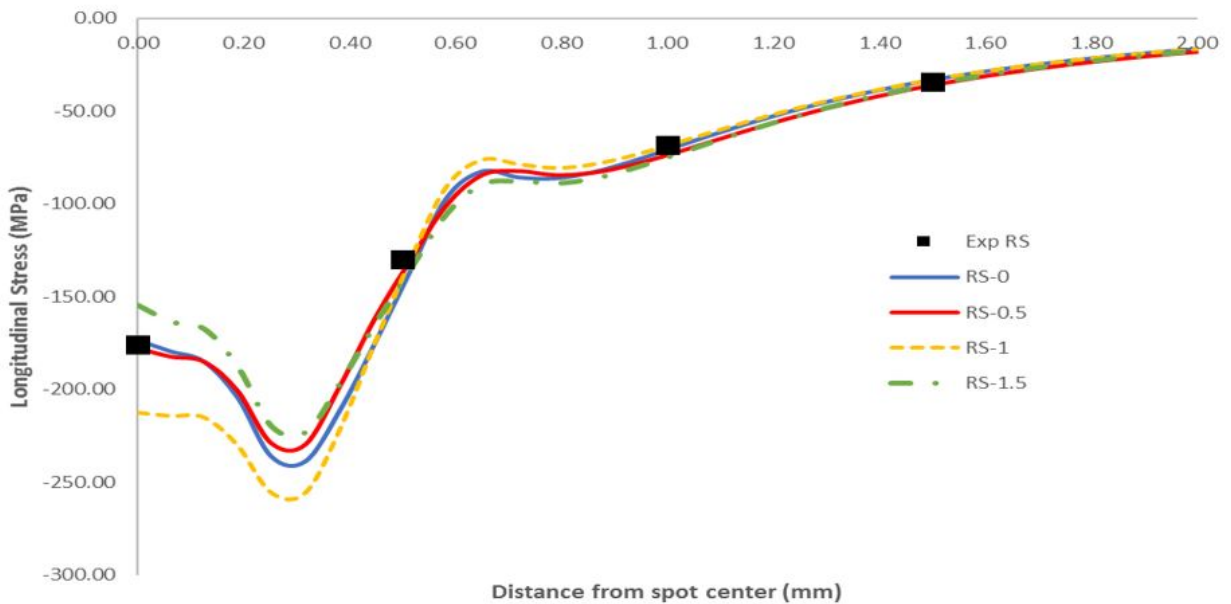


Figure 4.5. Longitudinal Stress - Radial Distribution for SLM Specimens

Although each residual stress curve representing a unique set of Johnson-Cook parameters (Table. 4.4) predict the assumed experimental residual stress at individual nodes at a radial distance of 0.5, 1 and 1.5 mm as seen in Fig. 4.5 and 4.6, none of the parameters predict the

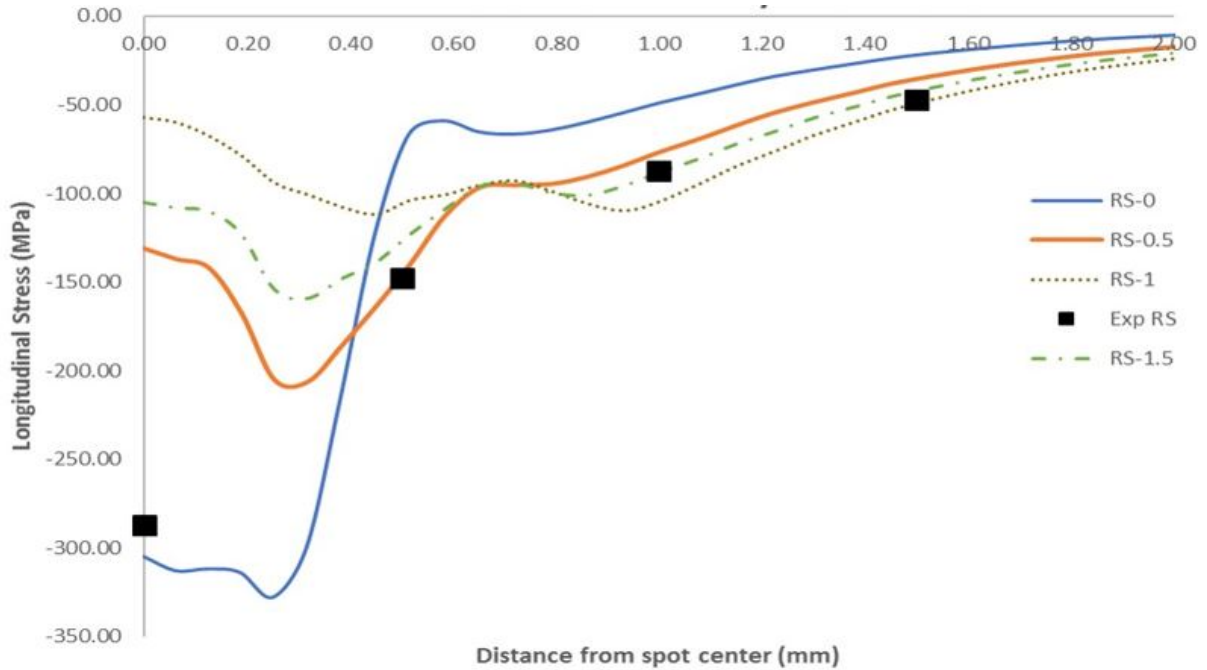


Figure 4.6. Longitudinal Stress - Radial Distribution for Casted Specimens

actual spatial stress field. Hence, a fine calibration of the Johnson-Cook parameters while also considering the experimental stress field is performed using Bayesian Inference.

A modified formulation for the posterior probability suggested in Eq. 4.6a and 4.6b employing the vectors $\sigma_{exp}^{\vec{}}$ and $\sigma_{res}^{\vec{}}$ depicting the experimental and residual field stresses is therefore used for fine calibration. The multidimensional Bayesian Inference calibrated Johnson-Cook parameters for the SLM and casted specimens are given in Table. 4.5.

Fig. 4.7 and 4.8 illustrates the residual stress prediction with these Johnson-Cook parameters. It is observed that the fine calibration considering multiple experimental dimensions results in accurate results for the SLM specimens and gives a reasonable result for the casted specimens. The resulting error between the assumed experimental and predicted residual stress is due to the accumulated errors in the spatial, temporal distribution of the laser profile and also the designed surrogate model. The Bayesian error is however calculated to be within 10% and hence the procedure can be further coupled to a probabilistic design

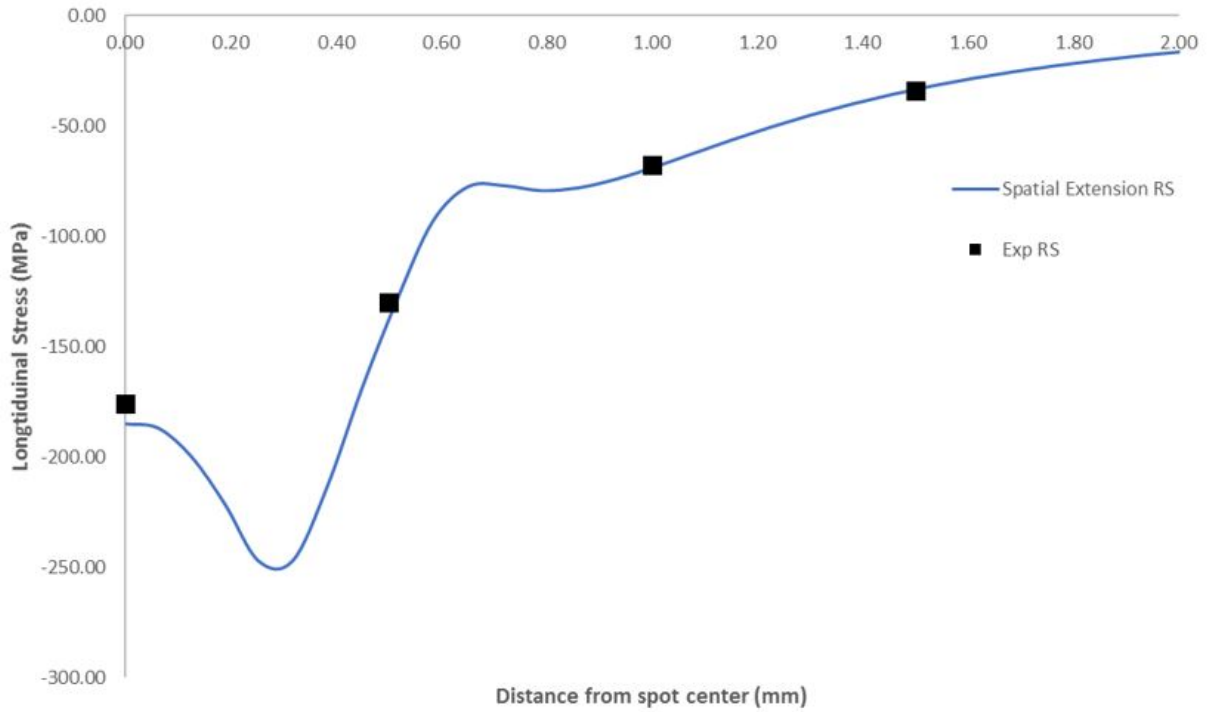


Figure 4.7. Longitudinal Stress for SLM Specimens with Spatially Calibrated JC Parameters

Table 4.5. Calibrated Johnson-Cook Parameters for the Residual Stress Field

| JC parameter | SLM | Casted |
|--------------|--------|--------|
| A (MPa) | 187.8 | 265.06 |
| B (MPa) | 257.6 | 257.6 |
| n | 0.1643 | 0.3045 |
| C | 0.0160 | 0.0196 |

optimization process for LSP induced stress field, given the actual experimental test results for the residual stresses.

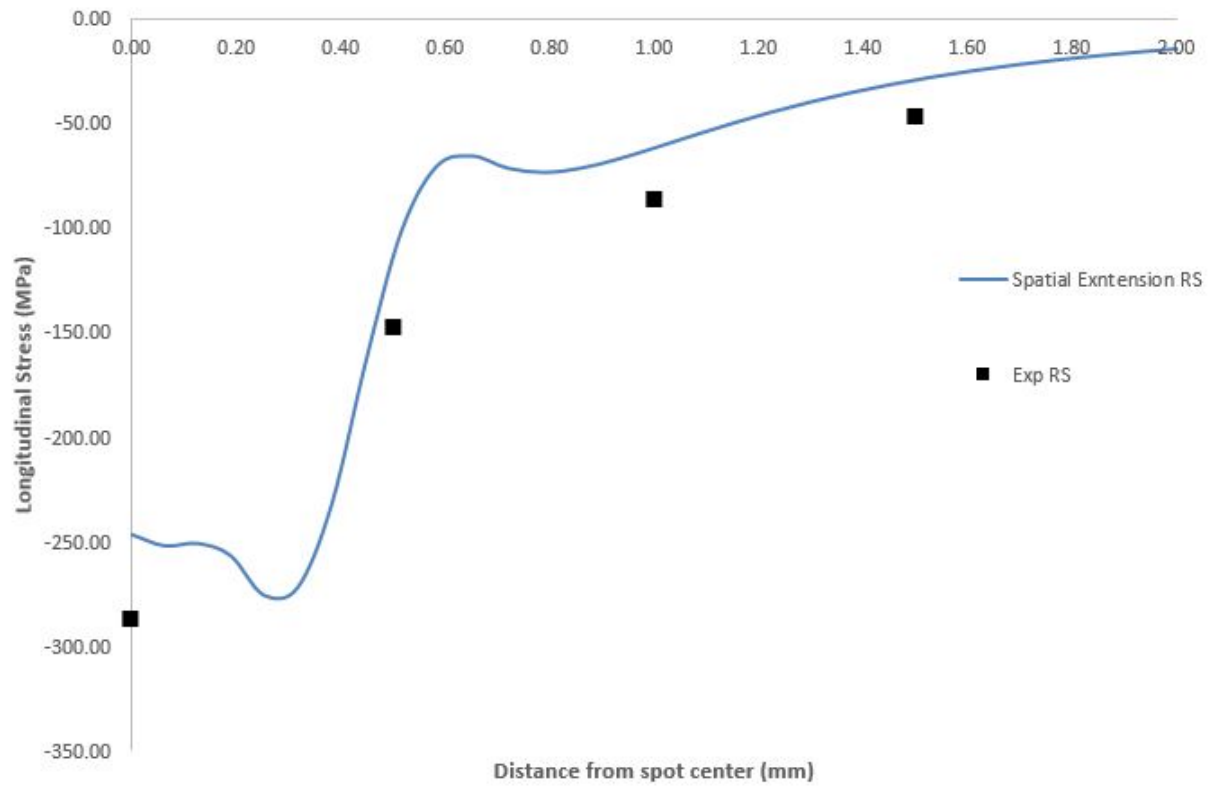


Figure 4.8. Longitudinal Stress for Casted Specimens with Spatially Calibrated JC Parameters

CHAPTER 5

RESIDUAL STRESS DISTRIBUTION FOR MULTIPLE LSP SHOTS

To differentiate the residual stress distribution between the SLM and casted A357 specimens, a candy-bar coupon previously shown in Fig. 2.1 is subjected to multiple laser shots. Two different patterns of LSP shots are designed and the SLM and casted specimens are laser peened with the configuration given in Table. 2.3. The laser peened specimens are then analyzed for the surface and in-depth residual stresses using x-ray diffraction.

Given the importance of residual stress distribution through the surface and depth, an attempt is made to develop two different laser peening patterns to maximize the compressive residual stress field in these directions. The first pattern is designed in such a way that the induced compressive stresses offer 100% coverage throughout the laser peened area. For this purpose, a series of 164 circular LSP shots are designed with 41 shots in each row with an approximate overlap of 50 %. The schematic of this pattern is shown in Fig. 5.1.

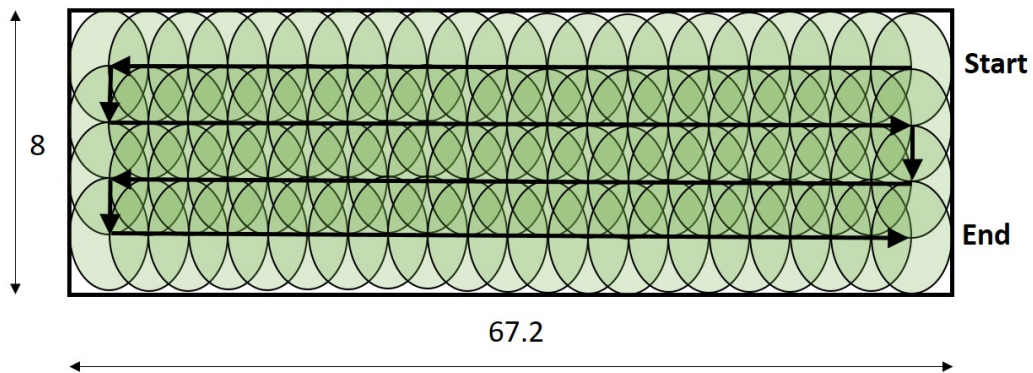


Figure 5.1. Pattern - 1 with circular LSP shots (100% coverage of laser peened area) (all dimensions are in *mm*)

The second LSP pattern is designed to study the penetration of induced compressive stresses through the depth of the specimen. Hence, 2 rows with 54 circular LSP shots are designed following the LSP path shown in in Fig. 5.2. Once the end point is reached, the specimen is processed again with a similar pattern to induce deeper compressive stresses.Hence

a total of 108 LSP shots are used for this pattern. The pattern configuration is summarized in Table. 5.1. The actual laser peened specimens with patterns 1 and 2 are shown in Fig. 5.3.

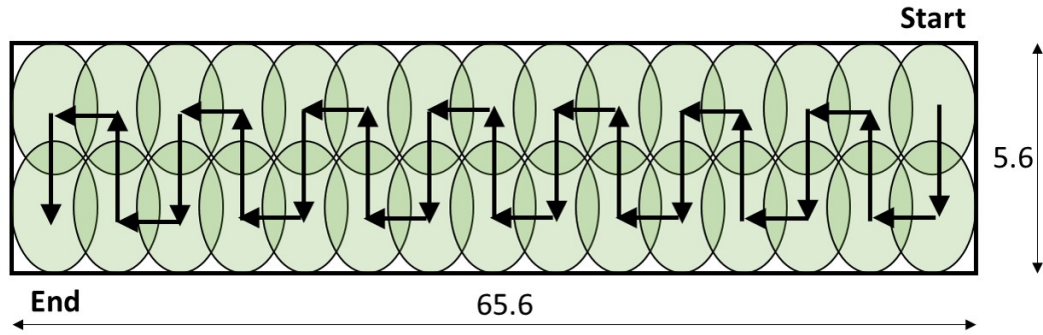


Figure 5.2. Pattern - 2 with circular LSP shots (Consecutive shots) (all dimensions are in *mm*)

Table 5.1. Laser Shock Peening - Pattern

| Parameter | Pattern-1 | Pattern-2 |
|-----------------------------|-----------|-----------|
| LSP shot shape | Circle | |
| Spot diameter (<i>mm</i>) | 3.2 | 3.2 |
| Overlap | 50 % | 25 % |
| Number of shots in a row | 41 | 27 |
| Number of rows | 4 | 2 |
| Total shots | 164 | 108 |

Following the experiment, the candybar coupon is modeled in *Abaqus/Explicit*. Since a repetition of residual stress distribution is expected along the surface, the working area is reduced to a small patch of 12 by 8 *mm* as depicted in Fig. 5.4. A suitable mesh is designed

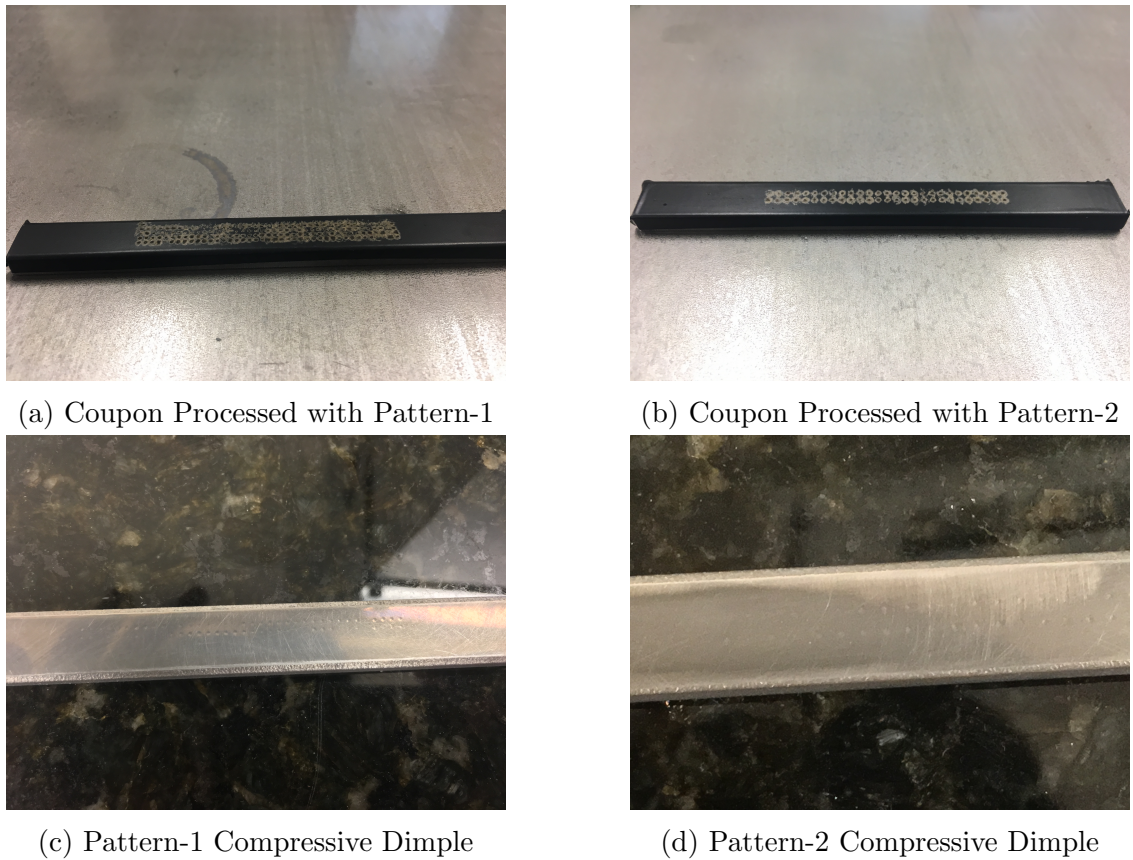


Figure 5.3. Laser Shock Peened Candybar Coupons

to simulate the LSP model with the calibrated Johnson-Cook parameters from Table. 4.5. Therefore, in this study, 22,28,604 temperature displacement coupled reduced integration elements (C3D8RT) with a uniform mesh spacing of $60 \mu m$ through the patch surface and $100 \mu m$ through the specimen depth is used.

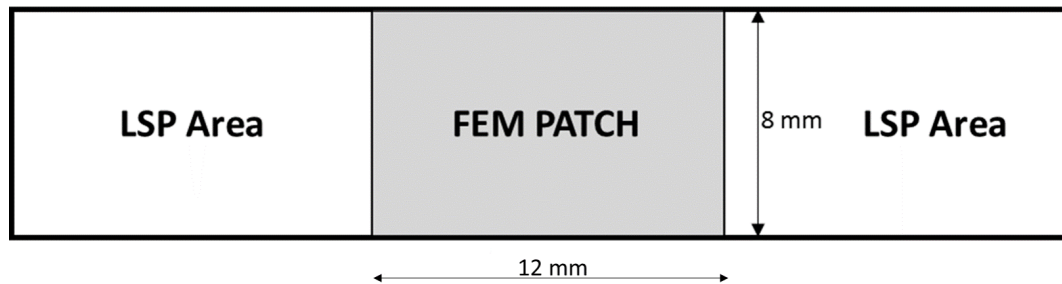


Figure 5.4. Candybar - FEM Simplification

For the current study, the distribution of residual stresses for different laser peening patterns shown in Fig. 5.1 and 5.2 is studied by simulating the candy-bar coupon in *Abaqus/Explicit* using the SEATD technique with the finite element formulation discussed above. The Johnson-Cook parameters for the SLM specimens given in Table 4.5 are used for pattern comparison.

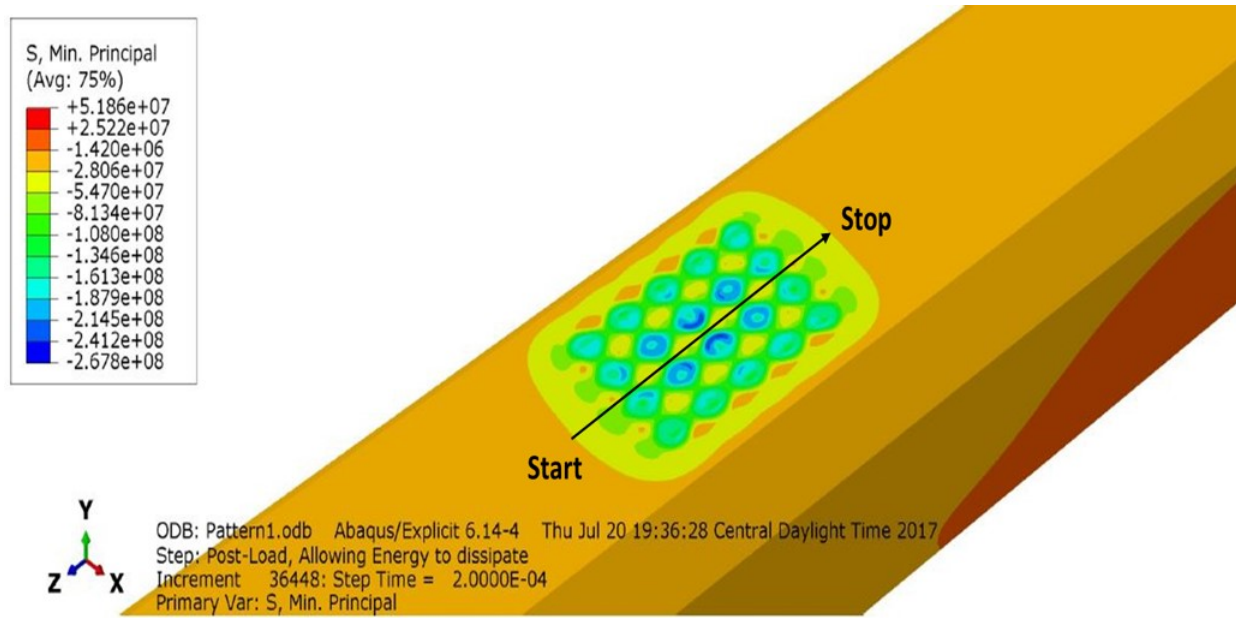


Figure 5.5. Compressive Stress Field due to Pattern-1

Fig. 5.5 and 5.6 illustrates the compressive field resulting due to LSP for Pattern-1. Although there are some tensile residual stresses observed in between laser shots, it is accounted for the Gaussian distribution of the laser beam. This necessitates the use of a higher overlap for subsequent work to guarantee 100% coverage of compressive stresses through the specimen surface area.

Fig. 5.7 and 5.8 depicts the in-depth compressive residual stress distribution on the candy-bar coupon subjected to LSP-Pattern 2. It is seen that the compressive stresses penetrate through a depth of 2.1 mm and hence the designed pattern indeed produces a deeper penetration of compressive stress field. A detailed comparison between SLM and

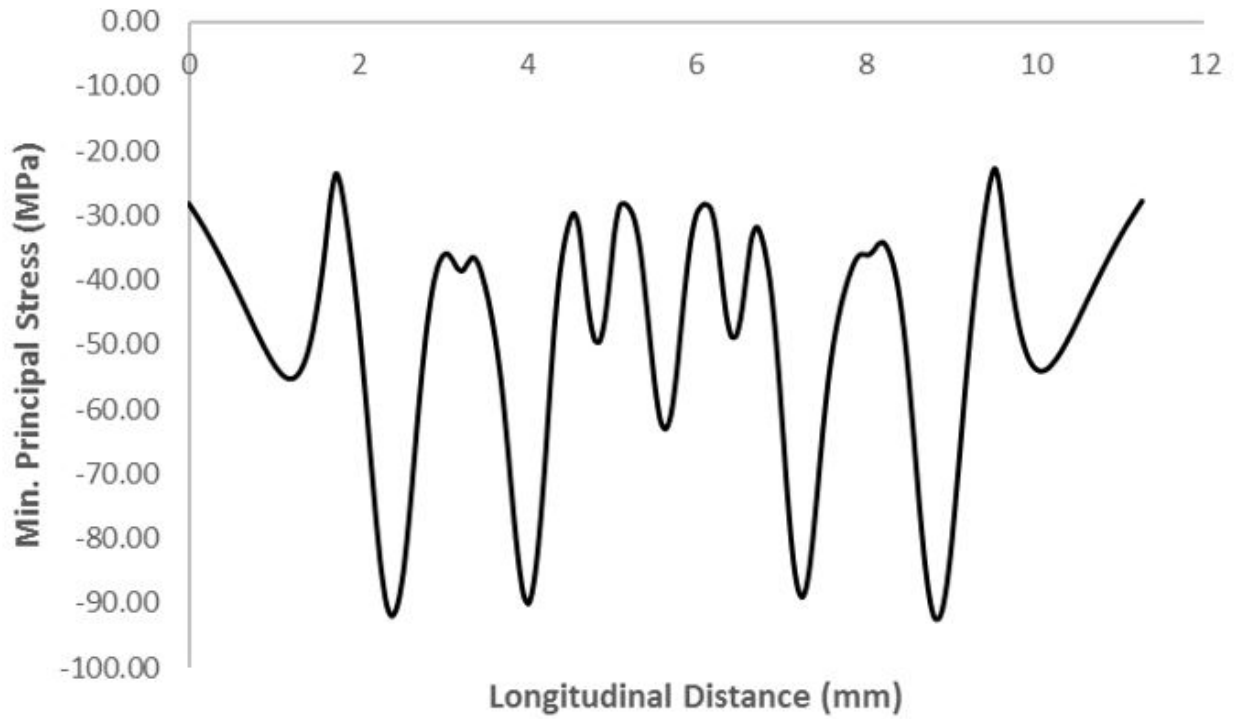


Figure 5.6. Residual Stress Distribution through the Path shown in Fig. 5.5

casted A357 specimens with the actual experimental residual stress field will be addressed in further studies.

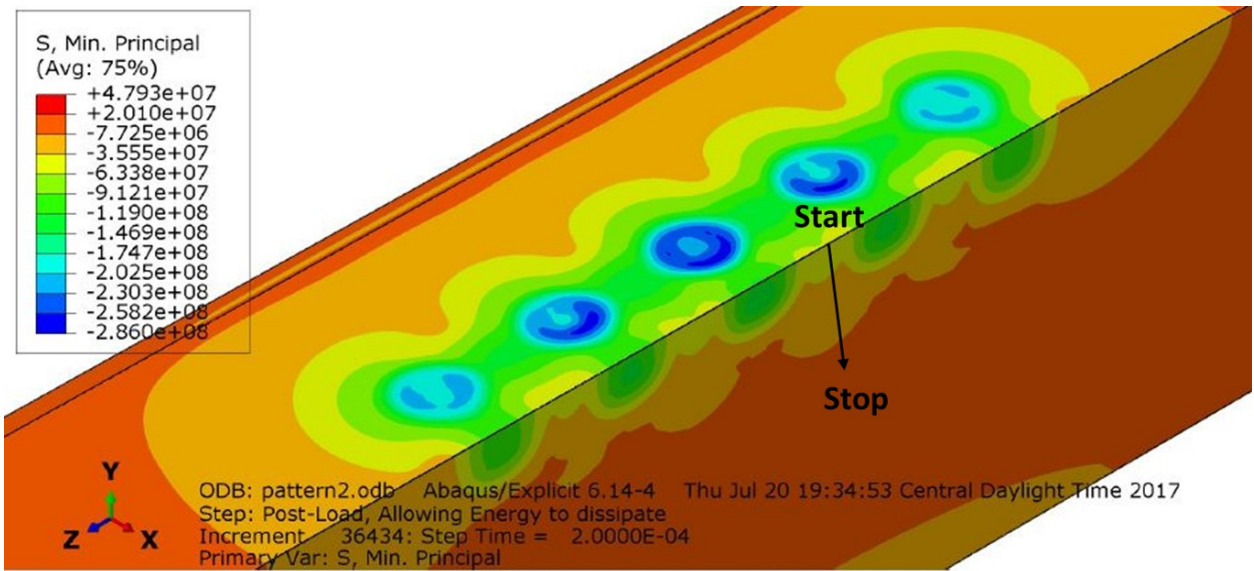


Figure 5.7. Compressive Stress Field due to Pattern-2

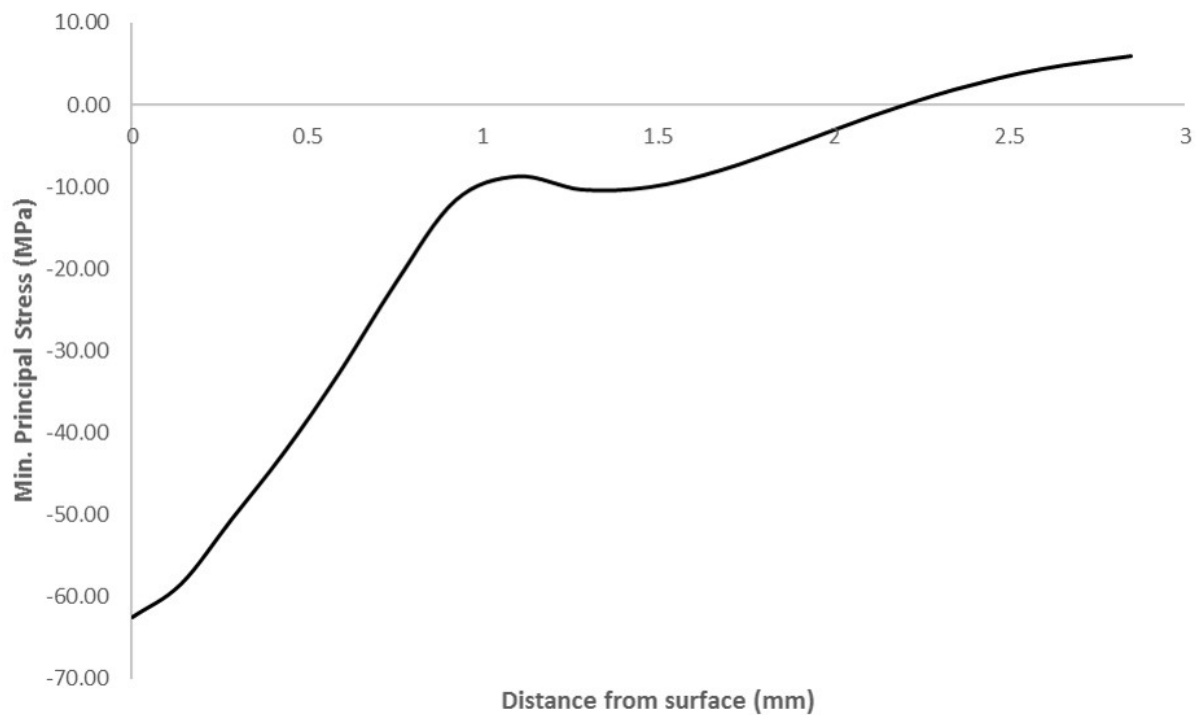


Figure 5.8. Residual Stress Distribution through the Path shown in Fig. 5.7

CHAPTER 6

CONCLUSION

Tensile residual stresses are developed in the A357-SLM specimens due to fluctuating temperature gradient reported during the heating-cooling phase in SLM and also due to the eutectic dispersion of silicon particles. Hence, to delay the crack nucleation and maximize the lifetime of SLM specimens under continuous and cyclic loads, two different configurations of laser shock peening is applied on SLM-A357 candy-bar coupons to counteract the existing tensile stresses. A favorable beam path to perform laser peening experiments is initially developed with the aid of high damage threshold laser optics. A new state of the art beam analysis device is used to obtain the spatial and temporal distribution of the laser pulse which is fed into all numerical simulations for laser peening. Additionally, to develop a reliable material model which can be further used in reliability based optimization of laser shock peening, a probabilistic approach called Bayesian Inference is introduced to calibrate the Johnson-Cook material model parameters at high strain rates. The Johnson-Cook parameters are further subjected to fine calibration by modifying the governing equation of Bayesian Inference to accommodate the residual stress field. The working technique of Bayesian Inference is demonstrated using a set of assumed experimental stress results. The Bayesian Inference-calibrated Johnson-Cook parameters are observed to predict the assumed residual stress field with a reasonably good accuracy. Finally, the influence of two laser peening patterns to achieve different compressive stress field on the candy-bar coupon is studied. The result indicates to employ an additional overlap for Pattern-1 to achieve 100% coverage of compressive stress field on the specimen surface area. Deeper compressive stresses are observed when the coupon is subjected to Pattern-2. Further studies would address the difference between the microstructure, residual stress distribution and fatigue life for the SLM and casted A357 specimens processed with similar laser peening treatment.

APPENDIX

EXPERIMENTAL APPARATUS

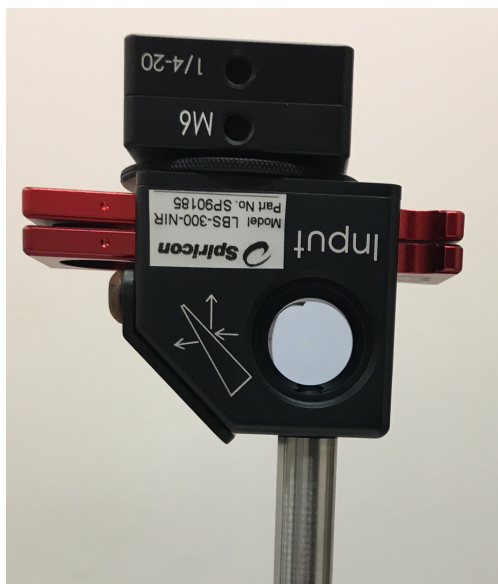
A.1 Beam Path

The laser system used in this work is the Quanta-Ray Spectra Physics Pro-350 high energy Nd:YAG laser. The laser produces a high fluence with a range of 40-50 J/cm^2 for a 3.5 mm diameter on the incident optics. Hence, high damage threshold laser line mirrors and lenses are used in this work to design the most optimal beam path for LSP.

Three NB1-K14 uncoated laser line mirrors with 1 inch outer diameter and 0 - 45° angle of incidence is used to reflect the 12.7 mm incident laser beam by 90°. The mirrors also have a high damage threshold of 140 J/cm^2 for a 3.5 mm spot to withstand high fluence while reflecting the beam to the working area. Since the near infrared (NIR) beam out of the laser system is observed to have significant divergence, the mirrors are placed as close to each other as possible to prevent any additional divergence due to beam reflection. Following the reflection from the laser line mirrors, the laser beam is allowed to pass through an anti-reflection coated, N-BK7 substrate, 2 inch plano-convex lens with a focal length of 400 mm. The grade C - anti-reflection coated positive lens prevents most of the back reflection from the working area to prevent any damage to the laser diode. The plano-convex lens used in this work has a very high damage threshold of 150 J/cm^2 for a 3.5 mm laser spot diameter and hence guarantees to withstand high power densities. The incident diverging laser beam through the positive lens converges at the focal point. At a distance of 15 mm past the focal point, the beam is observed to have a $1/e^2$ Gaussian diameter of 3.2 mm required for laser peening. For beam collimation, an uncoated, N-BK7 substrate, 2 inch plano-concave lens with a focal length of -75 mm is placed at a distance of 55 mm from the first lens. An uncoated plano-concave lens is used to withstand the high fluence of the incident laser beam due to the reduced spot diameter. The plano-concave lens is placed on a fine calibration ruler to vary the beam diameter whilst ensuring reasonable beam collimation.

A.2 Beam Splitter and Beam Tap

The collimated laser beam out of the plano-concave lens is allowed to pass through a beam-splitter for laser beam analysis. The beam splitter used in this study samples 1% of the incident laser beam and transmits the rest. The LBS-300 NIR beam splitter shown in Fig. A.1a has a damage threshold of only 1 J/cm^2 which is significantly low for the laser system used in this work. Hence, the laser is operated on the “single shot” mode rather than working on the “continuous” mode to decrease the incident power density as much as possible.



(a) LBS-300 NIR Beam Splitter with a C- mount camera



(b) Beam Tap 1 and 2

Figure A.1. Laser Spatial Distribution - Apparatus

The beam splitter used in this work has two outlets. One outlet is for transmitting 99% of the high energy laser beam to the working area. A high speed camera as shown in Fig. A.1a is placed at the second outlet. The sampled laser beam is further attenuated by two monochromatic filters which further reduces the laser intensity transmitted to the camera by 99 %. The camera measures the laser intensity and enables the user to visualize the 2-D

and 3-D laser beam using a beam analysis software called *BeamGage*. The output from the camera using *BeamGage* for an attenuated laser beam is shown in Fig. A.2.

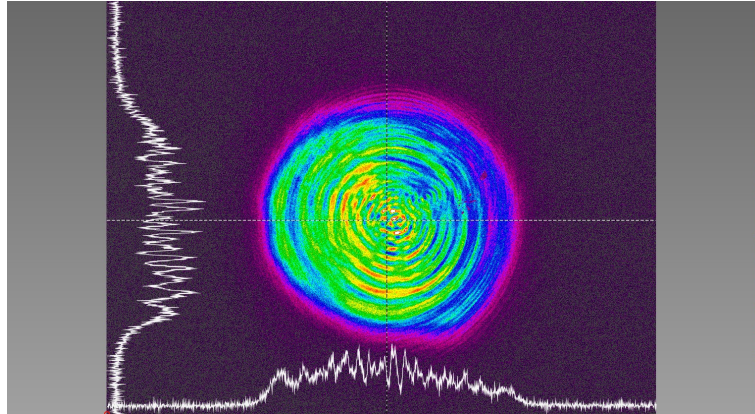


Figure A.2. Quanta-Ray Laser Beam Spatial Distribution using *BeamGage*

Since the laser pulse is observed to have similar spatial profiles for high power densities used in laser peening, the spatial distribution is not measured while performing the laser peening experiment. Hence, the weaker beam splitter is replaced with a high damage threshold beam tap, shown in Fig. A.1b. The coupled beam tap 1 and 2 used in this work has a high damage threshold of 1 MJ/cm^2 with 2 outlets. The beam tap is observed to reduce the laser intensity by 99.75 % at the second outlet making it useful for measuring the laser temporal distribution and laser energy.

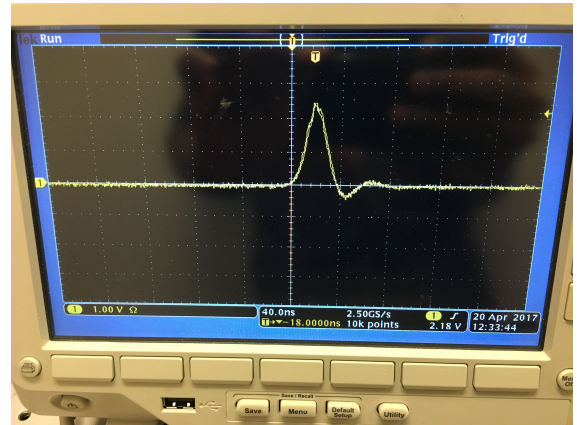
A.3 Fast Photodetector and Laser Energy Meter

The 0.25 % sampled laser beam out of the beam tap is used for measuring the useful pulse width and energy per laser pulse. The fast photodetector shown in Fig. A.3a is a photo sensor that captures the incident photons on the detector and converts it to a corresponding electrical pulse. This electrical pulse is read by an oscilloscope which in turn provides the temporal distribution of the laser pulse. Pulse saturation is observed when the 0.25% sampled laser beam is directly incident on the photo sensor. Hence, to prevent saturation and

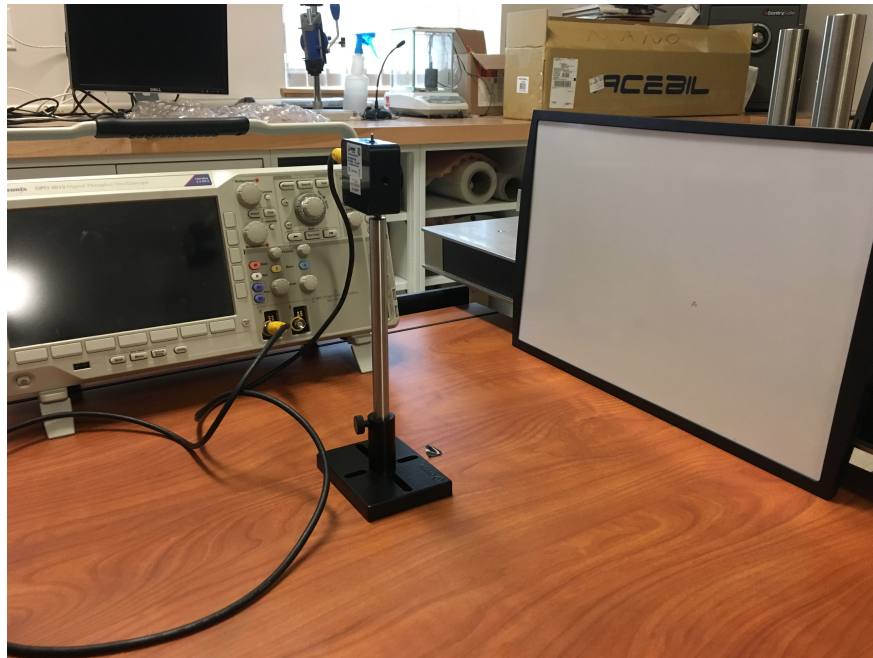
to avoid additional attenuation which might possibly result in complete beam absorption, the sampled laser beam is made incident on a white matte surface as shown in Fig. A.3c and the back scattering of the sampled laser pulse is caught by the sensor. Fig. A.3b illustrates the temporal distribution of the laser pulse on a high resolution oscilloscope.



(a) Fast Photo Detector



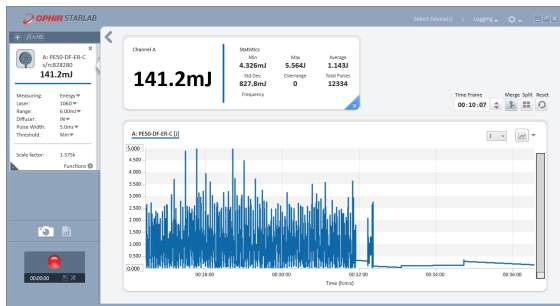
(b) Laser Pulse in Oscilloscope



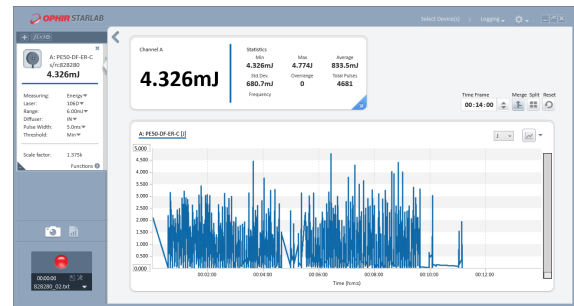
(c) Setup for Temporal Distribution

Figure A.3. Laser Temporal Distribution

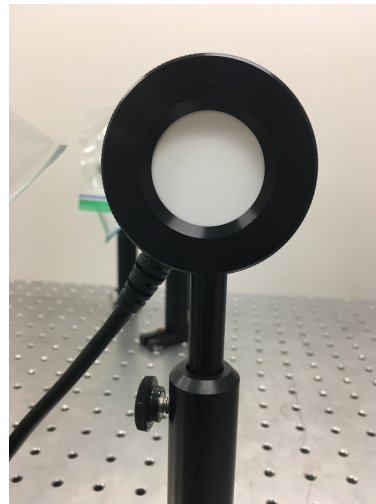
For continuous measurement of laser energy while performing the experiment, a high damage threshold laser energy meter with a diffuser shown in Fig. A.4c is used. The energy meter consists of a detection sensor to measure the intensity of the laser beam and is connected to an external computer to read the laser energy through the *StarLab* software. The laser energy meter and the measured laser energy for laser peening patterns 1 and 2 discussed in Chapter 5 is shown in Fig. A.4a and A.4b.



(a) Pattern-1 Measured Energy



(b) Pattern-2 Measured Energy



(c) Energy Meter

Figure A.4. Laser Energy

REFERENCES

- Aboulkhair, N. T., N. M. Everitt, I. Ashcroft, and C. Tuck (2014). Reducing porosity in AlSi10Mg parts processed by selective laser melting. *Additive Manufacturing* 1, 77–86.
- Agapovichev, A., V. Kokareva, V. Smelov, and A. Sotov (2016). Selective laser melting of titanium alloy: investigation of mechanical properties and microstructure. In *IOP Conference Series: Materials Science and Engineering*, Volume 156, pp. 012031. IOP Publishing.
- Alexopoulos, N. and S. G. Pantelakis (2004). Quality evaluation of A357 cast aluminum alloy specimens subjected to different artificial aging treatment. *Materials & design* 25(5), 419–430.
- Amarchinta, H. K., R. V. Grandhi, A. H. Clauer, K. Langer, and D. S. Stargel (2010). Simulation of residual stress induced by a laser peening process through inverse optimization of material models. *Journal of Materials Processing Technology* 210(14), 1997–2006.
- Arola, D., A. Alade, and W. Weber (2006). Improving fatigue strength of metals using abrasive waterjet peening. *Machining science and technology* 10(2), 197–218.
- ASTM-F2792 (2012). F2792-12a. *Standard Terminology for Additive Manufacturing Technologies*, ASTM International, West Conshohocken, PA 10, 2.
- Attar, H., M. Bönisch, M. Calin, L.-C. Zhang, S. Scudino, and J. Eckert (2014). Selective laser melting of in situ titanium–titanium boride composites: processing, microstructure and mechanical properties. *Acta Materialia* 76, 13–22.
- Aversa, A., M. Lorusso, F. Trevisan, E. P. Ambrosio, F. Calignano, D. Manfredi, S. Biamino, P. Fino, M. Lombardi, and M. Pavese (2017). Effect of process and post-process conditions on the mechanical properties of an A357 alloy produced via laser powder bed fusion. *Metals* 7(2), 68.
- Baumers, M., C. Tuck, R. Hague, I. Ashcroft, and R. Wildman (2010). A comparative study of metallic additive manufacturing power consumption. In *Solid freeform fabrication symposium, Austin, TX, Aug*, pp. 278–288.
- Bhamare, S., G. Ramakrishnan, S. R. Mannava, K. Langer, V. K. Vasudevan, and D. Qian (2013). Simulation-based optimization of laser shock peening process for improved bending fatigue life of Ti–6Al–2Sn–4Zr–2Mo alloy. *Surface and Coatings Technology* 232, 464–474.
- Braisted, W. and R. Brockman (1999). Finite element simulation of laser shock peening. *International Journal of Fatigue* 21(7), 719–724.

- Bremen, S., W. Meiners, and A. Diatlov (2012). Selective laser melting. *Laser Technik Journal* 9(2), 33–38.
- Brockman, R. A., W. R. Braisted, S. E. Olson, R. D. Tenaglia, A. H. Clauer, K. Langer, and M. J. Shepard (2012). Prediction and characterization of residual stresses from laser shock peening. *International Journal of Fatigue* 36(1), 96–108.
- Casavola, C., S. Campanelli, and C. Pappalettere (2008). Experimental analysis of residual stresses in the selective laser melting process. In *Proceedings of the XIth International Congress and Exposition, Orlando, Florida, USA*.
- Clauer, A. H. (1996). Laser shock peening for fatigue resistance. In *Proceedings of a Conference on Surface Performance of Titanium, At Cincinnati, OH*, Volume Surface Performance of Titanium, pp. 217–230. TMS, Warrendale, PA.
- Clauer, A. H., J. H. Holbrook, and B. P. Fairand (1981). Effects of laser induced shock waves on metals. In *Shock waves and high-strain-rate phenomena in metals*, pp. 675–702. Springer.
- Clauer, A. H., C. T. Walters, and S. C. Ford (1983). The effects of laser shock processing on the fatigue properties of 2024-T3 aluminum. In *Lasers in materials processing, Los Angeles, California*, pp. 7–22. American Society for Metals, Metals Park, Ohio.
- Ding, K. and L. Ye (2006). *Laser shock peening: performance and process simulation*. Woodhead Publishing.
- Emelogu, A., M. Marufuzzaman, S. M. Thompson, N. Shamsaei, and L. Bian (2016). Additive manufacturing of biomedical implants: A feasibility assessment via supply-chain cost analysis. *Additive Manufacturing* 11, 97–113.
- Fabbro, R., J. Fournier, P. Ballard, D. Devaux, and J. Virmont (1990). Physical study of laser-produced plasma in confined geometry. *Journal of applied physics* 68(2), 775–784.
- Fairand, B., B. Wilcox, W. Gallagher, and D. Williams (1972). Laser shock-induced microstructural and mechanical property changes in 7075 aluminum. *Journal of Applied Physics* 43(9), 3893–3895.
- Forrester, A., A. Keane, et al. (2008). *Engineering design via surrogate modelling: a practical guide*. John Wiley & Sons.
- Forrester, A. I. and A. J. Keane (2009). Recent advances in surrogate-based optimization. *Progress in Aerospace Sciences* 45(1), 50–79.
- Frazier, W. E. (2010). Direct digital manufacturing of metallic components: vision and roadmap. In *21st Annual International Solid Freeform Fabrication Symposium, Austin, TX, Aug*, pp. 9–11.

- Frazier, W. E. (2014). Metal additive manufacturing: a review. *Journal of Materials Engineering and Performance* 23(6), 1917–1928.
- Gupta, S., S. Abotula, and A. Shukla (2014). Determination of johnson–cook parameters for cast aluminum alloys. *Journal of Engineering Materials and Technology* 136(3), 034502.
- Hasser, P. J. (2014). *An efficient reliability-based simulation framework for optimum laser peening treatment*. Ph. D. thesis, Saint Louis University.
- Hasser, P. J., A. S. Malik, K. Langer, T. J. Spradlin, and M. I. Hatamleh (2016). An efficient reliability-based simulation method for optimum laser peening treatment. *Journal of Manufacturing Science and Engineering* 138(11), 111001.
- Hatamleh, M., J. Mahadevan, A. Malik, and D. Qian (2017). Variable damping for laser shock peening simulation using modal analysis and the SEATD method. In *Manufacturing Science and Engineering Conference (MSEC-2017), Los Angeles, California*. ASME.
- Hfaiedh, N., P. Peyre, H. Song, I. Popa, V. Ji, and V. Vignal (2015). Finite element analysis of laser shock peening of 2050-T8 aluminum alloy. *International Journal of Fatigue* 70, 480–489.
- Hibbitt, Karlsson, and Sorensen (2001). *ABAQUS/Explicit: User's Manual*, Volume 1. Hibbitt, Karlsson and Sorenson Incorporated.
- John, R., S. R. Thompson, and T. Nicholas (1999). Fatigue crack growth rate characteristics of laser shock peened Ti-6Al-4V. *J. Eng. Mater. Technol* 121, 321–329.
- Kalentics, N., E. Boillat, P. Peyre, S. Ćirić-Kostić, N. Bogojević, and R. E. Logé (2017). Tailoring residual stress profile of selective laser melted parts by laser shock peening. *Additive Manufacturing* 16, 90–97.
- Kalentics, N., E. Boillat, P. Peyre, C. Gorny, C. Kenel, C. Leinenbach, J. Jhabvala, and R. E. Logé (2017). 3d laser shock peening—a new method for the 3d control of residual stresses in selective laser melting. *Materials & Design* 130, 350–356.
- Kempen, K., L. Thijs, E. Yasa, M. Badrossamay, W. Verheecke, and J. Kruth (2011). Process optimization and microstructural analysis for selective laser melting of als10mg. In *Solid Freeform Fabrication Symposium*, Volume 22, pp. 484–495.
- Kim, J. H., Y. J. Kim, and J. S. Kim (2013). Effects of simulation parameters on residual stresses for laser shock peening finite element analysis. *Journal of Mechanical Science and Technology* 27(7), 2025–2034.
- Kruth, J.-P., J. Deckers, E. Yasa, and R. Wauthlé (2012). Assessing and comparing influencing factors of residual stresses in selective laser melting using a novel analysis method. *Proceedings of the institution of mechanical engineers, Part B: Journal of Engineering Manufacture* 226(6), 980–991.

- Kumar, G., S. Hegde, and K. N. Prabhu (2007). Heat transfer and solidification behaviour of modified A357 alloy. *Journal of Materials Processing Technology* 182(1), 152–156.
- Luong, H. and M. R. Hill (2008). The effects of laser peening on high-cycle fatigue in 7085-T7651 aluminum alloy. *Materials Science and Engineering: A* 477(1), 208–216.
- Murr, L., S. Gaytan, F. Medina, H. Lopez, E. Martinez, B. Machado, D. Hernandez, L. Martinez, M. Lopez, R. Wicker, et al. (2010). Next-generation biomedical implants using additive manufacturing of complex, cellular and functional mesh arrays. *Philosophical Transactions of the Royal Society of London A: Mathematical, Physical and Engineering Sciences* 368(1917), 1999–2032.
- Nelson, A. W., A. S. Malik, J. C. Wendel, and M. E. Zipf (2014). Probabilistic force prediction in cold sheet rolling by bayesian inference. *Journal of Manufacturing Science and Engineering* 136(4), 041006.
- Park, I., H. K. Amarchinta, and R. V. Grandhi (2010). A bayesian approach for quantification of model uncertainty. *Reliability Engineering & System Safety* 95(7), 777–785.
- Peyre, P., I. Chaieb, and C. Braham (2007). FEM calculation of residual stresses induced by laser shock processing in stainless steels. *Modelling and simulation in materials science and engineering* 15(3), 205.
- Peyre, P., A. Sollier, I. Chaieb, L. Berthe, E. Bartnicki, C. Braham, and R. Fabbro (2003). Fem simulation of residual stresses induced by laser peening. *The European Physical Journal Applied Physics* 23(2), 83–88.
- Rao, H., S. Giet, K. Yang, X. Wu, and C. H. Davies (2016). The influence of processing parameters on aluminium alloy A357 manufactured by selective laser melting. *Materials & Design* 109, 334–346.
- Rombouts, M., J.-P. Kruth, L. Froyen, and P. Mercelis (2006). Fundamentals of selective laser melting of alloyed steel powders. *CIRP Annals-Manufacturing Technology* 55(1), 187–192.
- Sathyajith, S., S. Kalainathan, and S. Swaroop (2013). Laser peening without coating on aluminum alloy Al-6061-T6 using low energy Nd: YAG laser. *Optics & Laser Technology* 45, 389–394.
- Sealya, M., G. Madireddy, C. Lib, and Y. Guob (2016). Finite element modeling of hybrid additive manufacturing by laser shock peening. In *Solid Freeform Fabrication 2016: Proceedings of the 27th Annual International Solid Freeform Fabrication System, Austin, TX*, Volume Solid Freeform Fabrication System.

- Selcuk, C. (2011). Laser metal deposition for powder metallurgy parts. *Powder Metallurgy* 54(2), 94–99.
- Shamsaei, N., A. Yadollahi, L. Bian, and S. M. Thompson (2015). An overview of direct laser deposition for additive manufacturing; part ii: Mechanical behavior, process parameter optimization and control. *Additive Manufacturing* 8, 12–35.
- Shiozaki, T., Y. Tamai, and T. Urabe (2015). Effect of residual stresses on fatigue strength of high strength steel sheets with punched holes. *International Journal of Fatigue* 80, 324–331.
- Singh, G. (2009). *Effective Simulation and Optimization of a Laser Peening Process*. Ph. D. thesis, Wright State University.
- Song, B., X. Zhao, S. Li, C. Han, Q. Wei, S. Wen, J. Liu, and Y. Shi (2015). Differences in microstructure and properties between selective laser melting and traditional manufacturing for fabrication of metal parts: A review. *Frontiers of Mechanical Engineering* 10(2), 111–125.
- Spierings, A., T. Starr, and K. Wegener (2013). Fatigue performance of additive manufactured metallic parts. *Rapid prototyping journal* 19(2), 88–94.
- Spradlin, T. J. (2011). *Process Sequencing for Fatigue Life Extension of Large Scale Laser Peened Components*. Ph. D. thesis, Wright State University.
- Sundar, R., H. Kumar, R. Kaul, K. Ranganathan, P. Tiwari, L. Kukreja, and S. Oak (2012). Studies on laser peening using different sacrificial coatings. *Surface Engineering* 28(8), 564–568.
- Trevisan, F., F. Calignano, M. Lorusso, E. Ambrosio, M. Lombardi, M. Pavese, and D. Manfredi (2016). Effects of heat treatments on a357 alloy produced by selective laser melting. In *Proceedings of the World PM 2016, Hamburg, Germany*.
- Trosch, T., J. Strößner, R. Völkl, and U. Glatzel (2016). Microstructure and mechanical properties of selective laser melted inconel 718 compared to forging and casting. *Materials letters* 164, 428–431.
- Turlach, B. A. et al. (1993). *Bandwidth selection in kernel density estimation: A review*. Université catholique de Louvain Louvain-la-Neuve.
- Wang, J., Y. Zhang, J. Chen, J. Zhou, M. Ge, Y. Lu, and X. Li (2015). Effects of laser shock peening on stress corrosion behavior of 7075 aluminum alloy laser welded joints. *Materials Science and Engineering: A* 647, 7–14.

- Yang, X., Z. Lai, J. Zhu, Y. Liu, and D. He (2012). Hot compressive deformation behavior of the as-quenched A357 aluminum alloy. *Materials Science and Engineering: B* 177(19), 1721–1725.
- Yang, X., J. Zhu, Z. Nong, Z. Lai, and D. He (2013). Fem simulation of quenching process in A357 aluminum alloy cylindrical bars and reduction of quench residual stress through cold stretching process. *Computational Materials Science* 69, 396–413.
- Zhang, D., L. Zheng, and D. StJohn (2002). Effect of a short solution treatment time on microstructure and mechanical properties of modified Al–7wt.% Si–0.3 wt.% Mg alloy. *Journal of Light Metals* 2(1), 27–36.
- Zhou, Z., S. Bhamare, G. Ramakrishnan, S. R. Mannava, K. Langer, Y. Wen, D. Qian, and V. K. Vasudevan (2012). Thermal relaxation of residual stress in laser shock peened Ti–6Al–4V alloy. *Surface and Coatings Technology* 206(22), 4619–4627.
- Zhou, Z., A. S. Gill, D. Qian, S. Mannava, K. Langer, Y. Wen, and V. K. Vasudevan (2011). A finite element study of thermal relaxation of residual stress in laser shock peened IN718 superalloy. *International Journal of Impact Engineering* 38(7), 590–596.

BIOGRAPHICAL SKETCH

Jagannathan S. Mahadevan is a Master's student in Mechanical Engineering department at The University of Texas at Dallas. His research interests include Structural mechanics of materials, Computational solid mechanics, Surface engineering and Reliability based optimization. He was recognized for his perfect GPA in graduate study with the competitive Erik-Jonsson Scholarship. He was hired as a Teaching Assistant in Spring 2016 and was consecutively reappointed for 3 successive long semesters. Prior to joining The University of Texas at Dallas, Jagannathan obtained his degree in Bachelor of Engineering, Mechanical Engineering from Anna University, Chennai, India. He has been the second author for two recently published research articles based on laser peening and is currently working as a first author for a research journal.

CURRICULUM VITAE

Jagannathan S. Mahadevan

July 28, 2017

Contact Information:

Department of Mechanical Engineering
The University of Texas at Dallas
800 W. Campbell Rd.
Richardson, TX 75080-3021, U.S.A.

Voice: (832) 273-5236
Email: jxs152330@utdallas.edu

Educational History:

B.E., Mechanical Engineering, Anna University, 2015

Mechanical and Tribological Behavior of Metal Matrix Aluminum Composite with Reinforcement Materials

Senior Undergraduate Project

Department of Mechanical Engineering, Anna University

Advisor: Dr. Edward Kennedy *Design and Fabrication of an External Attachment on a Machine Lathe*

Junior Undergraduate Project

Department of Mechanical Engineering, Anna University

Advisor: Dr. Govindaraju

Employment History:

Teaching Assistant, The University of Texas at Dallas, January 2016 – May 2017

Professional Recognitions and Honors:

Erik Jonsson Scholarship for excellence in academy, UTD, Spring '16, Fall '16, Spring '17